DTIC

Numerical Acoustic Hull Array Optimization

John P. Casey
Deliang Wu
Submarine Electromagnetic Systems Department

Naval Undersea Warfare Center Division
Newport, Rhode Island

DTIC QUALITY INSPECTED 4

20001002 040

REPORT DOCUMENTATION PAGE

Public reporting for this collection of information is estimated to average 1 hour per response, including the time for reviewing instructions, searching existing data sources, gathering and maintaining the data needed, and completing and reviewing the collection of information. Send comments regarding this burden estimate or any other aspect of this collection of information, including suggestions for reducing this burden, to Washington Headquarters Services, Directorate for Information Operations and Reports, 1215 Jefferson Davis Highway, Suite 1204, Arlington, VA 22202-4302, and to the Office of Management and Budget, Paperwork Reduction Project (0704-0188), Washington, DC 20503.

1. AGENCY USE ONLY (Leave blank)	2. REPORT DATE 1 August 2000	3. REPORT TYPE AND DATES COVERED

4. TITLE AND SUBTITLE

Numerical Acoustic Hull Array Optimization

5. FUNDING NUMBERS

6. AUTHOR(S)

John P. Casey
Deliang Wu

7. PERFORMING ORGANIZATION NAME(S) AND ADDRESS(ES)

Naval Undersea Warfare Center Division
1176 Howell Street
Newport, RI 02841-1708

8. PERFORMING ORGANIZATION REPORT NUMBER

TR 11,239

9. SPONSORING/MONITORING AGENCY NAME(S) AND ADDRESS(ES)

10. SPONSORING/MONITORING AGENCY REPORT NUMBER

11. SUPPLEMENTARY NOTES

12a. DISTRIBUTION/AVAILABILITY STATEMENT

Approved for public release distribution is unlimited.

12b. DISTRIBUTION CODE

13. ABSTRACT (Maximum 200 words)

An objective function for acoustic hull array design has been developed that optimizes the array's broadband detection capability. This objective function is based on maximizing the deflection coefficient of a classical square-law detector with a small signal-to-noise ratio. In this report, the objective function is applied to an optimization algorithm to determine the optimum weights for several line arrays that are located along the surface of an air-filled, fluid-loaded spherical elastic shell. In each example, only point sources of noise and single-beam designs are considered. The noise-only beamformer output spectra for the optimum weights are compared with the spectra for other shadings.

14. SUBJECT TERMS

Underwater Acoustics   Submarine Sonar Systems   Passive Acoustic Hull Sonar Arrays

15. NUMBER OF PAGES

64

16. PRICE CODE

17. SECURITY CLASSIFICATION OF REPORT UNCLASSIFIED	18. SECURITY CLASSIFICATION OF THIS PAGE UNCLASSIFIED	19. SECURITY CLASSIFICATION OF ABSTRACT UNCLASSIFIED	20. LIMITATION OF ABSTRACT SAR

NSN 7540-01-280-5500

TABLE OF CONTENTS

LIST OF ILLUSTRATIONS

LIST OF TABLES

NUMERICAL ACOUSTIC HULL ARRAY OPTIMIZATION

1. INTRODUCTION

Traditional approaches to acoustic hull array design have focused on the optimization of desirable beam pattern properties such as the maximization of array gain or the minimization of sidelobe levels (references 1-3). Unfortunately, such traditional design approaches are applicable at only a single frequency. In general, the fundamental design goal for a passive acoustic hull array is an optimal broadband detection capability. To achieve this goal, an optimal hull array design procedure based on a broadband-detection criterion is required.

A revolutionary approach to large-scale submarine acoustic hull array design that focuses on the optimization of the beamformer response has recently been developed by Streit and Wettergren (reference 4). This approach is based upon maximizing the deflection coefficient of a classical square-law detector under the assumption of a small signal-to-noise ratio (SNR). Streit and Wettergren have derived an expression for the variance of the output of a square-law detector whose input is the beamformer output. The noise-only output variance (of the detector) is the theoretical basis of the objective function, which is appropriate for either correlated or uncorrelated noise sources that can be distributed either discretely or over a continuum. This objective function accounts for noise sources, beamforming effects, and structural-acoustic energy transfer of offending disturbances. (The theoretical development of the objective function and its gradient are given in reference 4.)

In this report, the optimal hull array design approach of Streit and Wettergren is applied to obtain the optimum element weight distributions for several line arrays. Although Streit and Wettergren have formulated the optimization problem to address single-beam as well as multiple-beam designs, only single-beam designs are considered. In the examples described here, only point sources of noise are considered. In the case of several noise sources, the excitations are assumed to be uncorrelated. In contrast, the responses of the array hydrophones are generally correlated with respect to each other. The power spectra of the noise sources considered are assumed to be uniform over each frequency band of interest. The results are obtained for arrays that are conformal with an air-filled, fluid-loaded spherical elastic shell. A spherical shell is used here because analytical expressions exist for the velocity and pressure fields (references 5-6).

A nonlinear optimization algorithm is applied to obtain numerical results for the optimal hull array design. Results are obtained for line arrays that operate over both low- and high-frequency bands, which correspond to element spacings of a small fraction of a wavelength and one-quarter to one-half of a wavelength, respectively. In addition, the noise-only beamformer output spectra are plotted and compared for optimum, uniform, and cosine-tapered weights.

2

2. DESCRIPTION OF OPTIMIZATION PROBLEM

Consider a hull array consisting of M hydrophones that are steered to receive an incoming plane wave in the direction described by the unit vector $\hat{\xi}_l$. Under low SNR conditions, the deflection coefficient d for the beam steered in the look direction $\hat{\xi}_l$ is directly proportional to the ratio of the total signal power in that beam to the standard deviation of the square-law detector output waveform (under the noise-only hypothesis) (reference 4). Under the assumptions that $\hat{\xi}_l$ is exactly the signal-arrival direction, that the incoming plane wave excites only the hydrophones and not the hull, and that the angular response of each hydrophone is omnidirectional with a flat spectral response, Streit and Wettergren (reference 4) have shown that the optimum deflection coefficient is found by solving the following minimization problem:

$$\min_{\underline{w} \in R^M} \int_{f_{min}}^{f_{max}} V^2(f; \underline{w}, \hat{\xi}_l) \, df , \tag{1}$$

subject to the linear equality constraint

$$\sum_{m=1}^{M} w_m = 1 , \tag{2}$$

and the non-negative constraint on the hydrophone weights

$$w_m \geq 0 , \quad m = 1, 2, ..., M . \tag{3}$$

In equation (1), f is the frequency in Hertz (Hz), the frequency band $f_{min} \leq f \leq f_{max}$ denotes the bandwidth of the receiver, $\underline{w} = [w_1, w_2, ..., w_M]^T$ is the column vector of element (hydrophone) weights, and V denotes the (noise only) beamformer output spectrum. The objective function in equation (1) is proportional to the variance of the output of the square-law detector under the noise-only hypothesis. It should be noted that equation (1) is a modification of the objective function derived by Streit and Wettergren (reference 4) and is more suitable for obtaining numerical results. The derivation of equation (1) from the original objective function in reference 4 is given in appendix A. Formulas for the components of the gradient of the objective function are also given in appendix A.

The optimization problem involves a nonlinear objective function subject to a linear equality constraint. The unknown real variables in equation (1) are the M hydrophone weights

3

w_m, $m = 1, 2, ..., M$, expressed in terms of an M-dimensional real vector $\underline{w}$. Numerical results for the optimization model are obtained through use of the nonlinear programming algorithm NPSOL developed at Stanford University (reference 7). NPSOL uses a sequential quadratic programming (SQP) algorithm in which the search direction is the solution of a quadratic programming (QP) subproblem. SQP algorithms are generally superior to gradient descent methods because they exhibit a higher rate of convergence in the vicinity of the solution (references 8 and 9). In addition, an SQP algorithm is well suited to this application because the objective function is quartic in the element weights. NPSOL has been successfully applied in the beam pattern optimization of conformal antenna arrays (reference 10).

A FORTRAN 77 driver program was written to apply NPSOL to the acoustic hull array optimization problem. For a given array, the driver program reads in the array element coordinates and the spectral Green's function (or transfer function) associated with a given noise source at various frequencies across the band of interest. The driver program then calls NPSOL, resulting in an optimum set of weights. The optimization results are validated by checking them for various starting points. In the present optimization problem, the objective function and its gradient are evaluated via numerical integration. The method of overlapping parabolas integration rule (reference 11) is applied here in order to perform the integration in the case where the spectral Green's functions are obtained at unequally spaced frequencies. A derivation of the overlapping parabolas integration rule is given in appendix B. A comparison of the performance of the overlapping parabolas rule with the trapezoidal and Simpson's rules is also given in appendix B.

3. POINT-EXCITED, FLUID-LOADED SPHERICAL SHELL

This report considers an air-filled, fluid-loaded spherical elastic shell of radius a and shell thickness h as shown in figure 1. The sphere is excited by a time-harmonic point force located at the north pole of the sphere. For the examples considered in this report, the diameter of the sphere is 15 ft ($a = 7.5$ ft $= 2.286$ m) and the shell thickness to radius ratio h/a is 0.011. The spherical geometry was chosen because analytical formulas can be derived for the velocity and pressure fields. Two array examples are examined here, i.e., a line array centered at the antipode ($\theta = 180°$), as shown in figure 2a, and a line array centered at $\theta = 140°$, as shown in figure 2b.
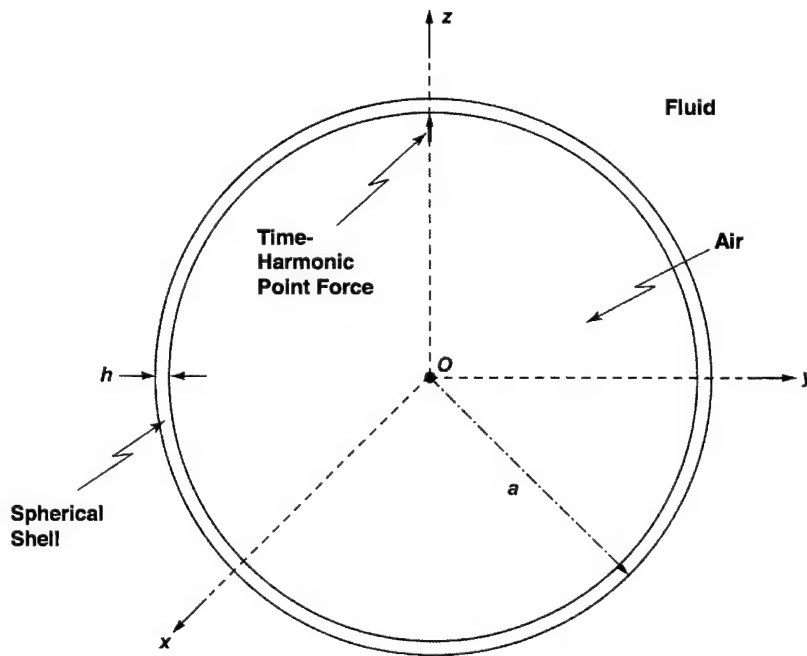
Figure 1. Point-Excited, Air-Filled, Spherical Elastic Shell in a Fluid

A set of MATLAB® programs has been written by Professor Peter Stepanishen of the University of Rhode Island to compute the velocity and pressure fields for an in-vacuo, or fluid-loaded, spherical elastic shell (air filled) that is excited by a time-harmonic point force located at the north pole of the shell (figure 1) (reference 6). Of particular importance to the beamformer optimization code (used to generate the results presented in this report) is the pressure field along the surface of the elastic shell. The transfer function $H(f; \boldsymbol{p}_m, \boldsymbol{q}_k, \hat{\zeta}_k)$, which is defined in appendix A, is the surface pressure at a point $\boldsymbol{p}_m$ on the shell surface that is produced by a time-harmonic (at a frequency f) point force located at a point $\boldsymbol{q}_k$ on the surface of the shell and oriented along the $\hat{\zeta}_k$ direction.
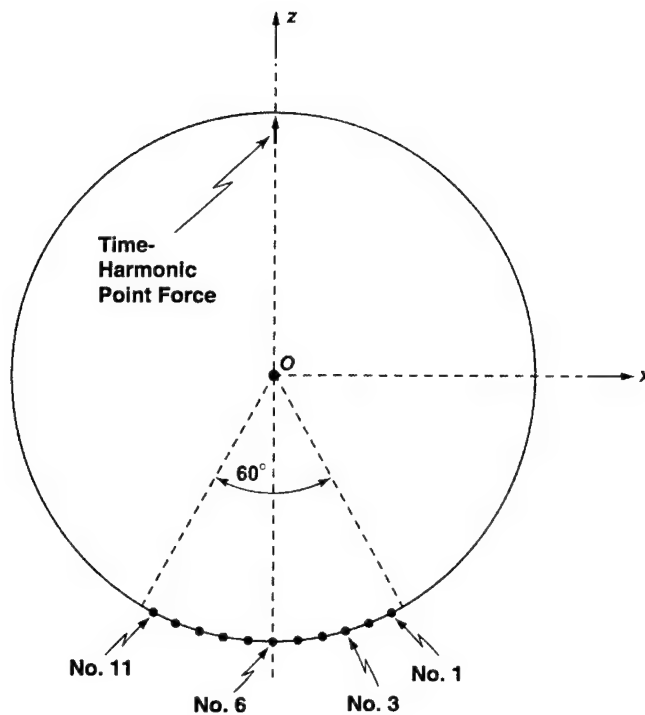
Figure 2a. Eleven-Element Line Array Centered at the South Pole ($\theta = 180°$) of Sphere
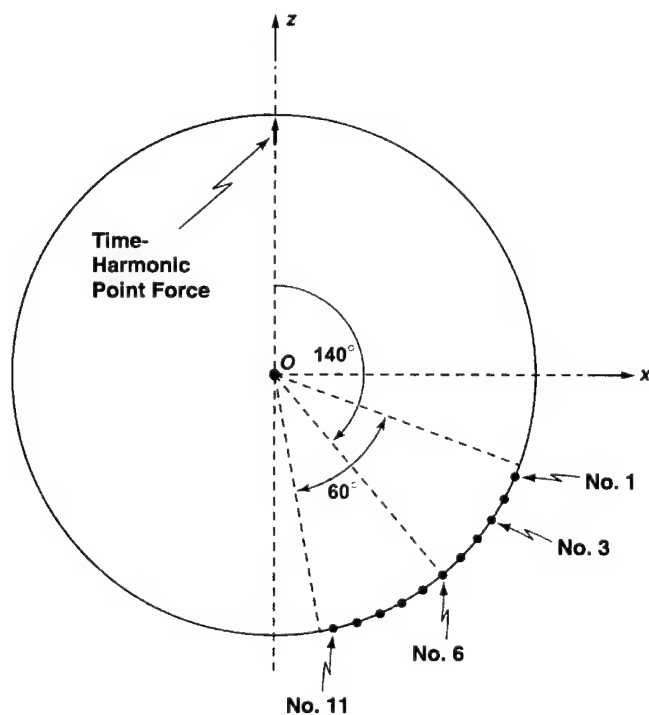
Figure 2b. Eleven-Element Line Array Centered at $\theta = 140°$

Stepanishen's MATLAB programs were developed for two purposes, i.e., to provide results for the validation of a finite-element code that is required for producing transfer functions for a more general geometry and to generate the transfer functions needed for the optimization results presented in this report. The MATLAB programs implement some analytical formulas for the structural-acoustic velocity and pressure fields that are expressed in terms of eigenfunction expansions.

The analytical formulas for the velocity field of the shell and the corresponding pressure field that are implemented in the MATLAB programs were derived by Stepanishen and Wettergren (reference 6). These formulas result from the solutions of the equations of motion for the shell. The normalized equations of motion for the shell, when immersed in a fluid, can be expressed as (reference 6)

$$\begin{bmatrix} L_{11} & L_{12} \\ L_{21} & L_{22} \end{bmatrix} \begin{bmatrix} U(x) \\ W(x) \end{bmatrix} - \Omega^2 \begin{bmatrix} U(x) \\ W(x) \end{bmatrix} = \frac{a}{h} \begin{bmatrix} F^u(x) \\ F^w(x) \end{bmatrix} - \frac{a}{h} \begin{bmatrix} 0 \\ P(x) \end{bmatrix} , \tag{4}$$

where $x = x(a,\theta)$ denotes a point on the middle surface of the spherical shell and θ denotes the polar angle in spherical coordinates. The terms L_{mn} denote partial differential operators in spherical coordinates while $U(x)$ and $W(x)$ represent the in-plane and normal displacements, respectively, of the middle surface of the shell. A steady-state time-harmonic field dependence $e^{i\Omega t}$ has been assumed in equation (4), where $\Omega = 2\pi f a/c_p$ is the normalized frequency, c_p is the speed of sound in the shell, and $i = \sqrt{-1}$. The force density terms $F^u(x)$ and $F^w(x)$ in equation (4) represent the mechanical excitations on the shell while $P(x)$ denotes the acoustic pressure that acts on the shell as a result of the nonzero normal velocity of the shell.

For a point-force excitation at $\theta = 0$ (figure 1), the force density terms in equation (4) are

$$F^u(x) = 0 , \tag{5a}$$

$$F^w(x) = \frac{F_o \delta(\theta)}{2\pi \sin \theta} , \tag{5b}$$

where F_o denotes the amplitude of the force and δ denotes the Dirac delta function. Substituting the excitations (5a) and (5b) into equation (4), Stepanishen and Wettergren have shown (reference 6) that the surface pressure can be expressed as

$$P(x) = i \frac{\rho_o c_o}{\rho_p c_p} \sum_{s=0}^{\infty} \frac{(2n+1)/2}{Z_n^M + Z_n} P_s(\cos \theta) \frac{h_s(\Omega c_p/c_o)}{h'_s(\Omega c_p/c_o)} , \tag{6}$$

where ρ_o and ρ_p denote the densities of air and the shell, respectively, c_o is the speed of sound in air, Z_n is the modal radiation impedance, Z_n^M is the total modal mechanical impedance, P_s is the Legendre polynomial of order s, and h_s and h'_s are the spherical Hankel function (of the first or second kind) and its derivative, respectively. Formulas for Z_n and Z_n^M are given in reference 6. Stepanishen and Wettergren have shown that their formulas are equivalent to the existing classical formulas given in Junger and Feit (reference 5).

Expression (6) neglects structural damping. Without structural damping, the denominator of equation (5) will vanish at each resonant frequency Ω_c, resulting in an unrealistic infinite surface pressure. Small losses can be accounted for through the multiplication of the speed of sound in the shell c_p by $1 + i\eta_s$, where η_s represents the structural damping or loss factor, with $\eta_s \ll 1$ (reference 5). The effect of the replacement of c_p by $c_p(1 + i\eta_s)$ in equation (6) is the removal of resonant frequencies from the real frequency axis and, thus, remove the singularities from the pressure field. According to Stepanishen (reference 12), typical values for the structural damping factor range from 0.01 to 0.1.

The effect of structural damping on the integrand of the objective function $V^2(f; w, \hat{\xi}_l)$ over two different frequency bands is shown in figures 3a and 3b . In these plots, $V^2(f; w, \hat{\xi}_l)$ was computed for the line array described in figure 2a with uniform weights and a beam steered at the look angle $\theta_l = 180°$. Figure 3a shows the integrand plot over the low-frequency band ($250\text{ Hz} \le f \le 1000\text{ Hz}$) while figure 3b applies to the high-frequency band ($1723\text{ Hz} \le f \le 3446$ Hz). The plots indicate the existence of numerous resonances across both frequency bands. Attempts to evaluate the objective function over either frequency band with no structural damping did not produce a convergent result. The plots show that for very small damping ($\eta_s = 0.01$) the resonances are attenuated significantly. Most of the resonant peaks are removed from $V^2(f; w, \hat{\xi}_l)$ for a structural damping factor of 0.05. This damping factor will be used in the examples that follow, because the integrand plots over both frequency bands are fairly smooth.

Expression (6) involves an infinite summation over the various modes of the spherical elastic shell. Stepanishen and Wettergren (reference 6) have determined that 150 modes (terms in the summation) are more than sufficient for convergence of the velocity and pressure fields over the frequency bands of interest.

8
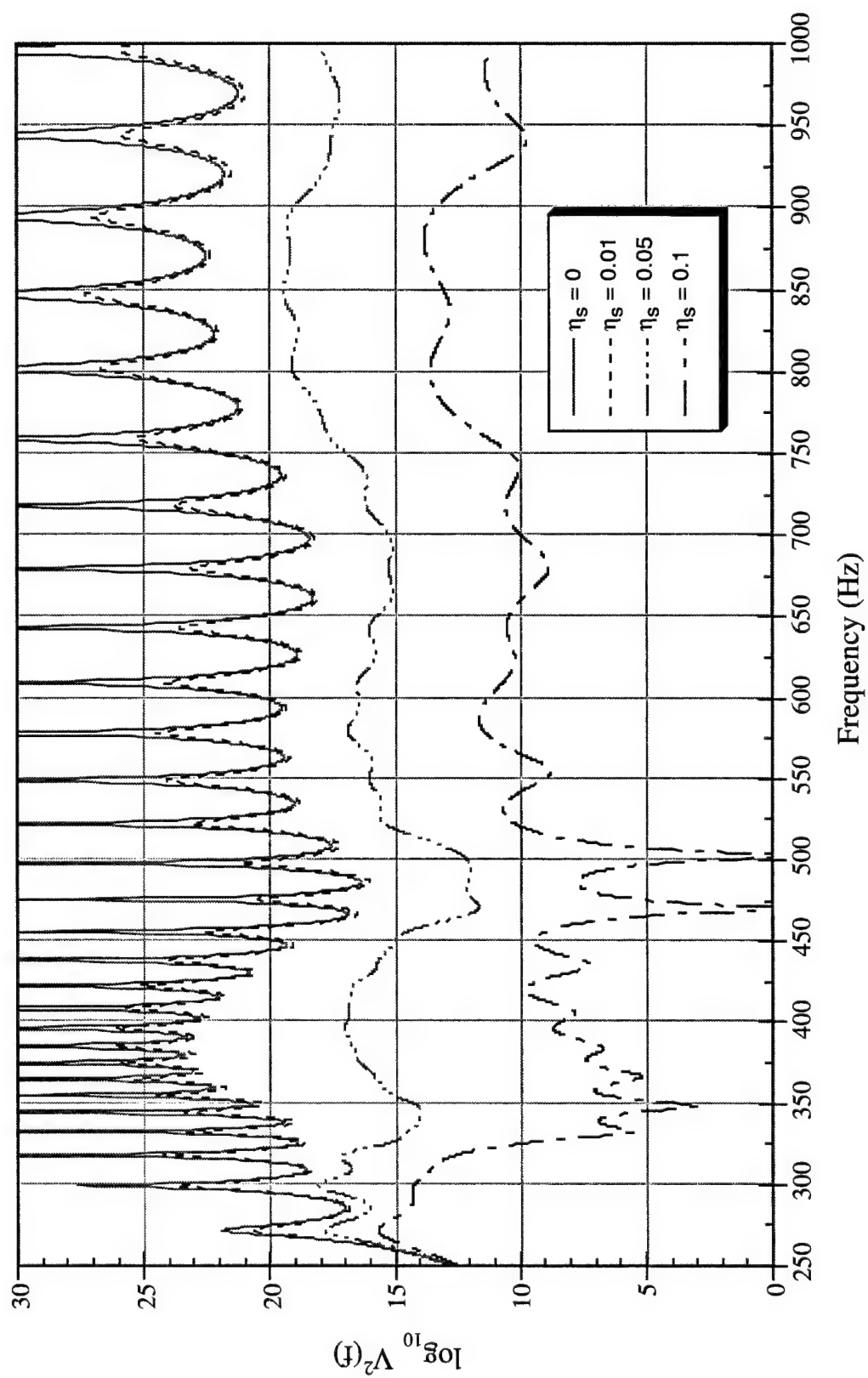
Figure 3a. *Integrand of the Objective Function over the Low-Frequency Band for the Line Array Described in Figure 2a with Uniform Weights and a Beam Steered at the Look Angle* $\theta_l = 180°$

9
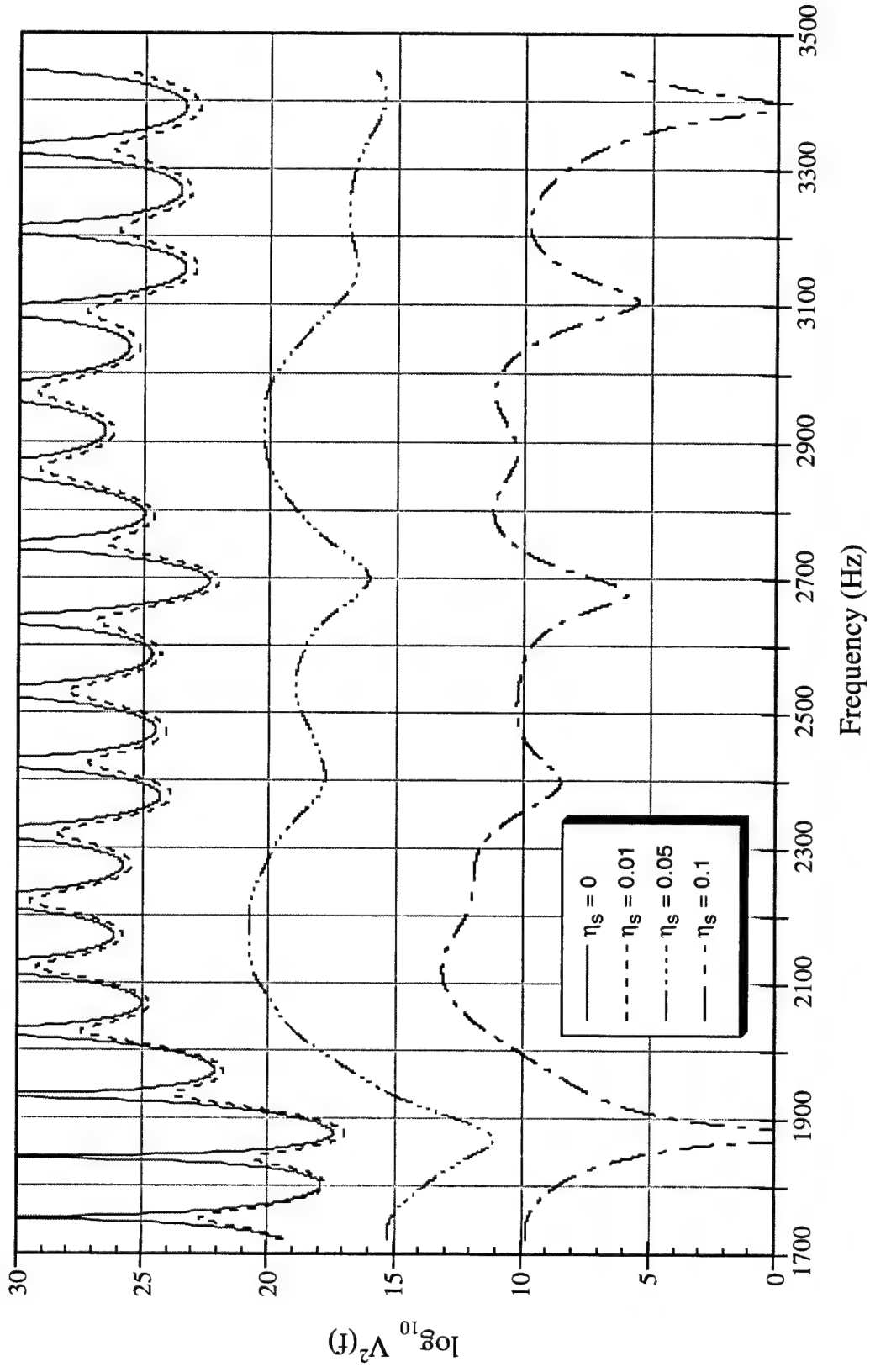
Figure 3b. Integrand of the Objective Function over the High-Frequency Band for the Line Array Described in Figure 2a with Uniform Weights and a Beam Steered at the Look Angle $\theta_l = 180°$

4. OPTIMIZATION RESULTS

The 11-element line array considered here is conformal to the surface of the 15-ft diameter air-filled, fluid-loaded spherical shell described in figure 1. The array elements are equally spaced and extend across a 60° arc along the sphere. For computational convenience, the array is placed along the xz-plane. As previously stated, two cases are considered in this report: the line array centered at the antipode ($\theta = 180°$) as shown in figure 2a and the line array centered at $\theta = 140°$ as shown in figure 2b. The $\theta = 140°$ case was chosen because the array has no element located at the antipode. In each example, the spherical shell has a time-harmonic point force (noise source) located at $\theta = 0°$.

The optimization of each array is performed over two different frequency bands. Over the low-frequency band of 250 Hz $\leq f \leq$ 1000 Hz, the spacing s between elements is $0.036\lambda \leq s \leq 0.145\lambda$, where λ is the acoustic wavelength in the fluid. The speed of sound in the fluid is 1500 m/s. The high-frequency band of 1723 Hz $\leq f \leq$ 3446 Hz was chosen so that the element spacing is $\lambda/4 \leq s \leq \lambda/2$. In each example considered, the optimum weight distribution will be plotted along with the corresponding noise-only beamformer output spectrum.

4.1 EXAMPLES FOR LOW-FREQUENCY BAND (250 Hz $\leq f \leq$ 1000 Hz)

In considering the 11-element line array centered at $\theta = 180°$ with a time-harmonic point force located at $\theta = 0°$, it is noted that the resulting transfer function magnitude plots at the locations of elements 1 to 3 and elements 4 to 6, are shown in figures 4a and 4b, respectively. Because the transfer function is axisymmetric for a point source located at $\theta = 0°$, the transfer functions for elements 7 to 11 are not plotted. Of particular importance in figures 4a and 4b is that the transfer function at the center element (no. 6) is noticeably larger than at the other element locations across most of the frequency band. This peculiarity is attributed to the fact that it lies at the antipodal point with respect to the source, which will have a noticeable impact on the optimization results as described below.

Figure 5a is a bar graph of the optimum weight distribution for the line array in figure 2a for a beam steered at the look angle $\theta = 180°$. The weight distribution is unusual because the minimum weight is at the center element. This can be attributed to the large transfer function magnitude at the center element location over most of the frequency band. Because the objective

11

function and gradient terms are on the order of 10^3 for the optimization of the line arrays in figures. 2a and 2b, they are each multiplied by 10^{-3} in the optimization program so that they are on the order of unity. This scaling of the objective function has no impact on the optimum solution; it only improves the numerical convergence. It should also be noted that the scaling factor for the objective function varies with each example.

The weight distribution in figure 5a is symmetric with respect to the center element. This same result was obtained for several feasible starting points (i.e., initial weight distributions that lie in the allowable domain as defined in equations (2) and (3)). However, it was observed that some infeasible starting points resulted in the same optimum objective value but different optimum weight distributions than the one in figure 5a. The reason for this peculiarity is that the transfer function and the array are each symmetric with respect to the beam-steering angle $\theta_l = 180°$. Consequently, the same objective function value is obtained for different element weight distributions such that the sums of the weights of opposing elements with respect to the center element are the same. This can be expressed mathematically as

$$w_n + w_{12-n} = c_n, \quad n = 1, 2, 3, 4, 5. \tag{7}$$

In equation (7), the c_n's are constants. If the weights are further constrained to be symmetric with respect to the center element, the optimum distribution in figure 5a will be obtained for both feasible and infeasible starting points.

Figure 5b is the optimum weight distribution for the line array in figure 2a for a beam steered at the look angle $\theta_l = 150°$. The weight distribution still has a minimum at the center element, but it is asymmetrical with respect to the array center. Note that relatively larger weights are on the side of the array in which the beam is steered, as expected. The same optimum weight distribution was obtained for both feasible and infeasible starting points.

Figure 6 shows the line array centered at $\theta = 180°$ with three time-harmonic point forces that are each diametrically opposite with respect to one of the three center elements (numbers 5 to 7). Note that the three forces are in phase and of equal amplitude. The purpose of this exercise is to see if the optimum weights produced at element numbers 5 and 7 are significantly reduced from those in figures 5a and 5b. Figures 7a and 7b illustrate the optimum weight distributions for beams steered at the look angles $\theta_l = 180°$ and $\theta_l = 150°$, respectively. The graphs show the expected results, i.e, that any element that is located at an antipodal point with respect to a point source will have a small optimum weight.

12
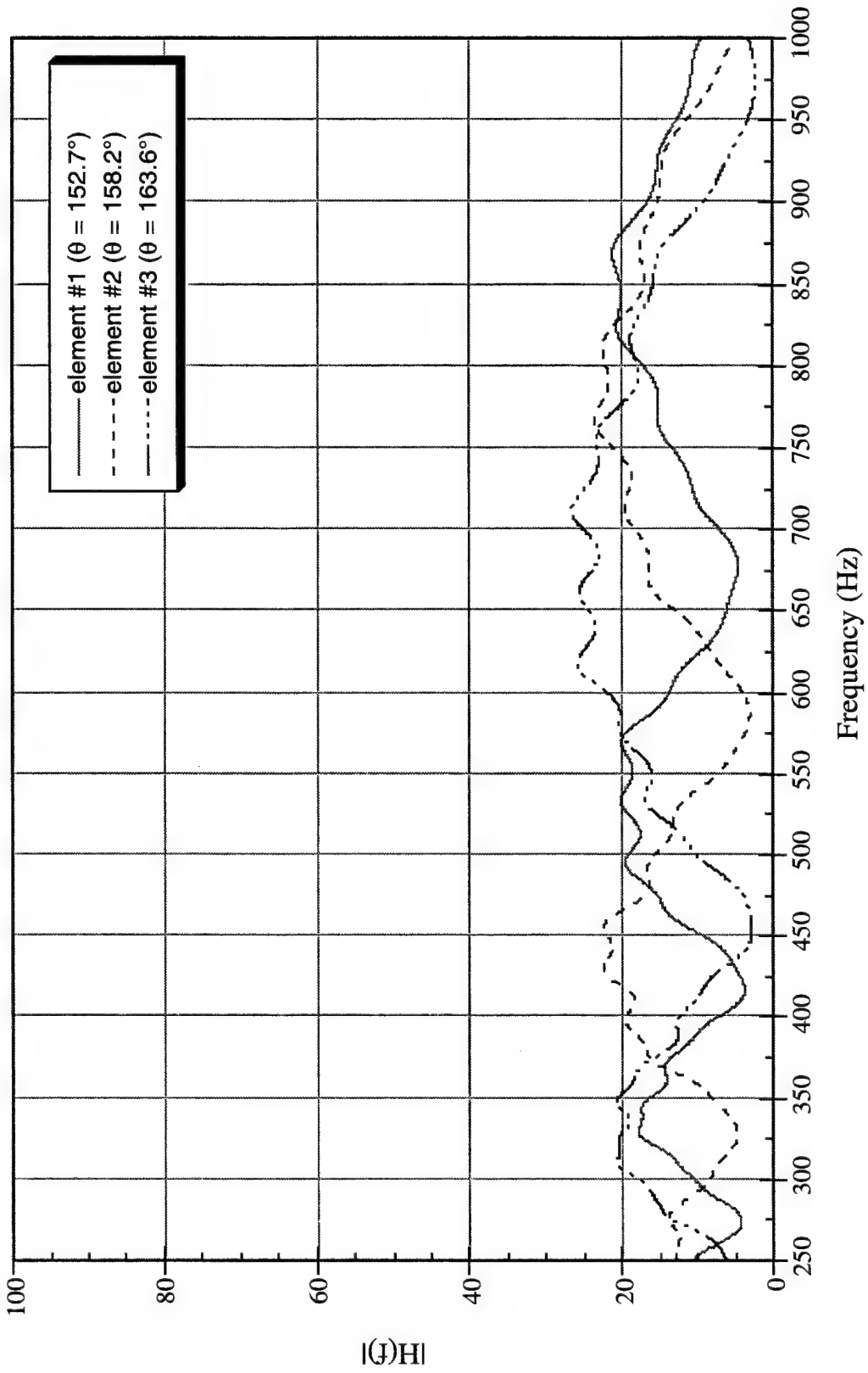
Figure 4a. Transfer Functions over the Low-Frequency Band at the Locations of Elements 1 to 3 for the Array Described in Figure 2a

13
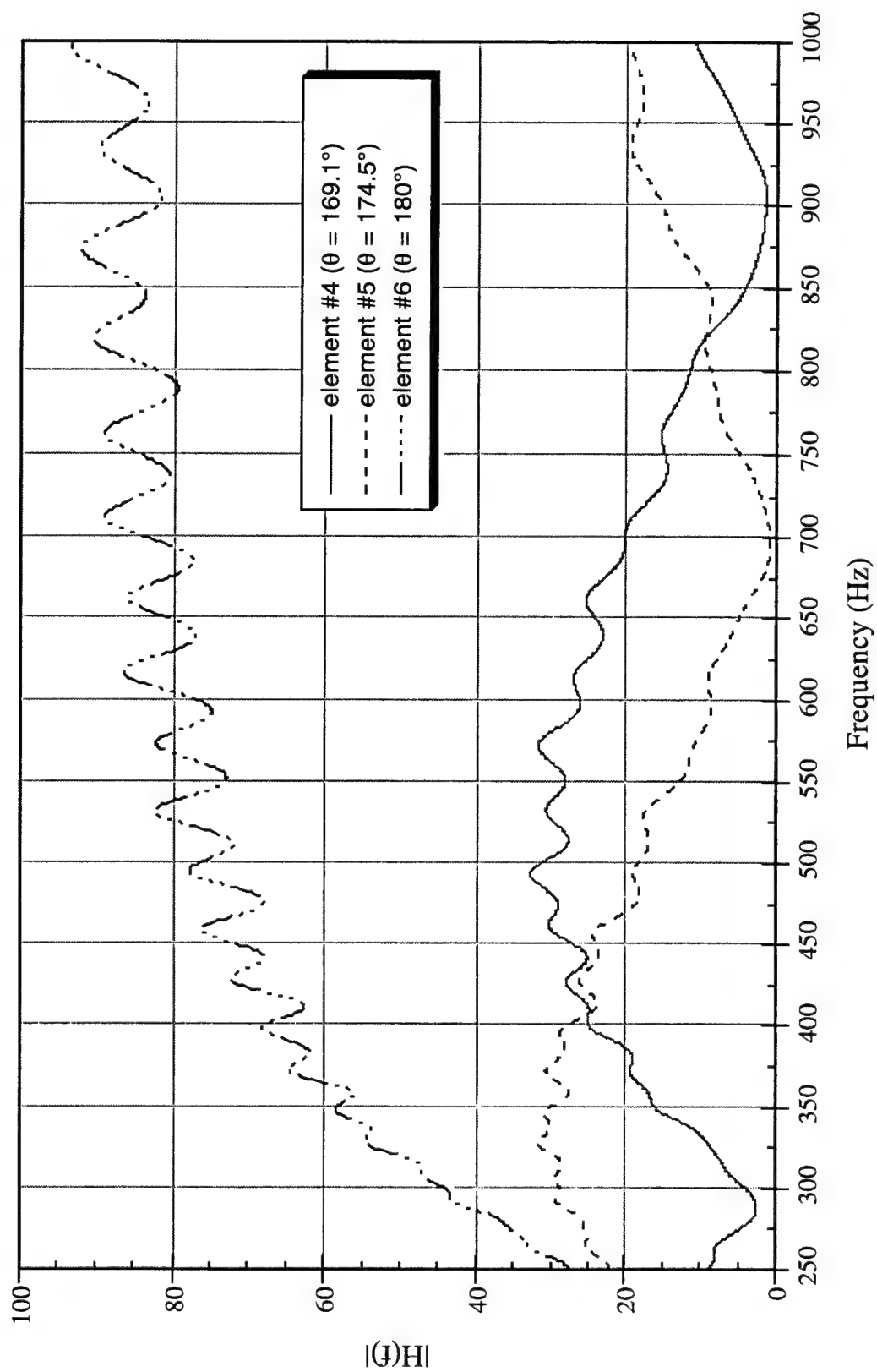
Figure 4b. Transfer Functions over the Low-Frequency Band at the Locations of Elements 4 to 6 for the Array Described in Figure 2a

14
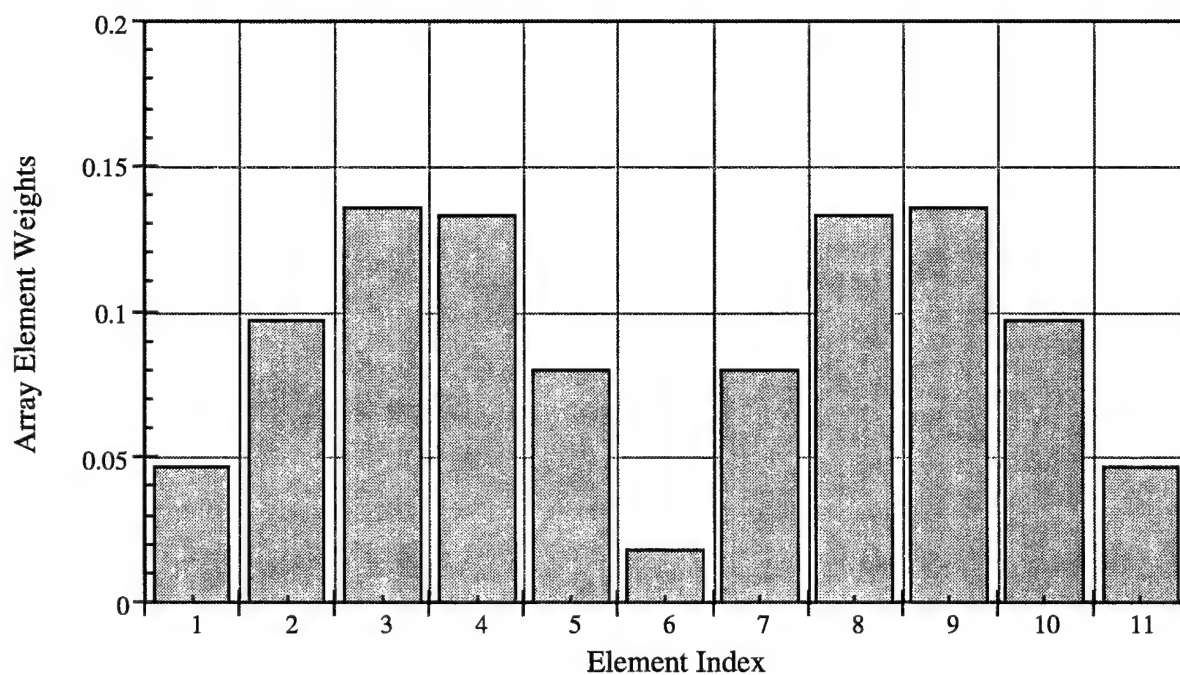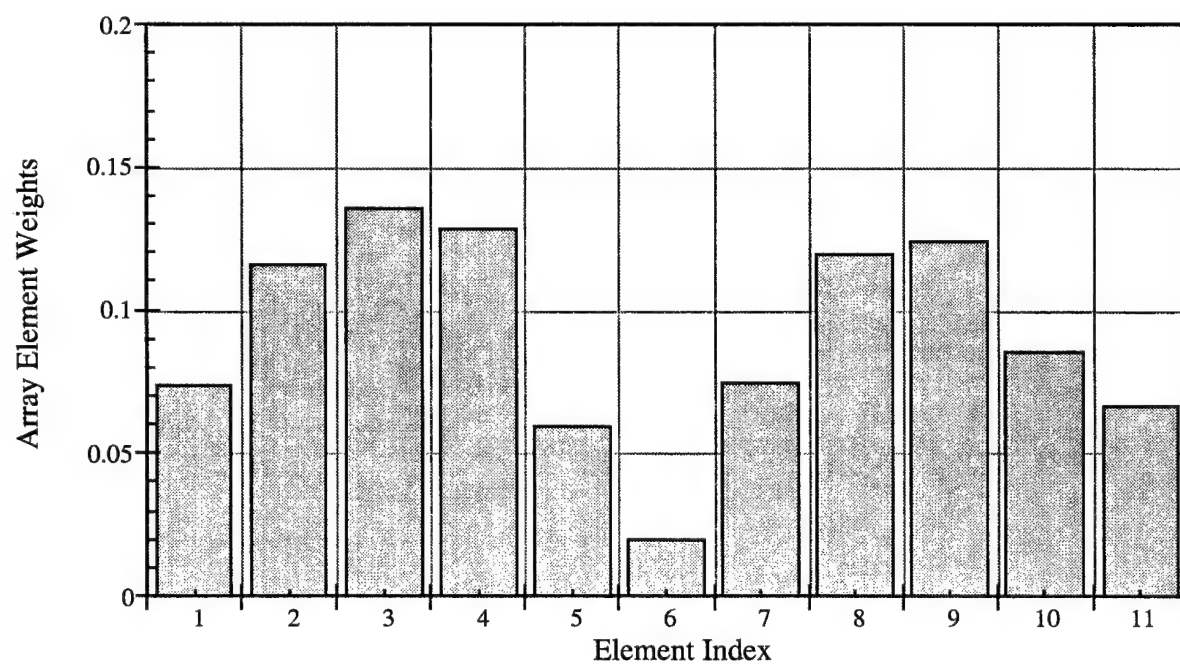
(a) $\theta_l = 180°$

(b) $\theta_l = 150°$

Figure 5. Optimum Weight Distributions for the 11-Element Line Array Described in Figure 2a over the Low-Frequency Band (250 Hz $\leq f \leq$ 1000 Hz) for Beam-Steering Angles (a) $\theta_l = 180°$ and (b) $\theta_l = 150°$

15
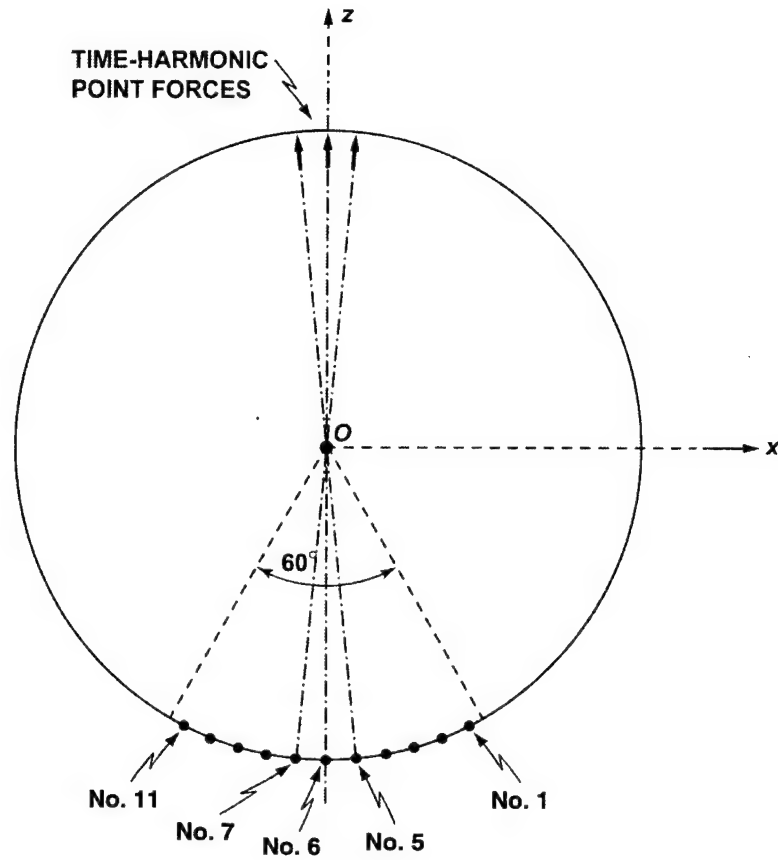
Figure 6. Eleven-Element Line Array Centered at the South Pole ($\theta = 180°$) of the Sphere with Three Time-Harmonic Point Forces
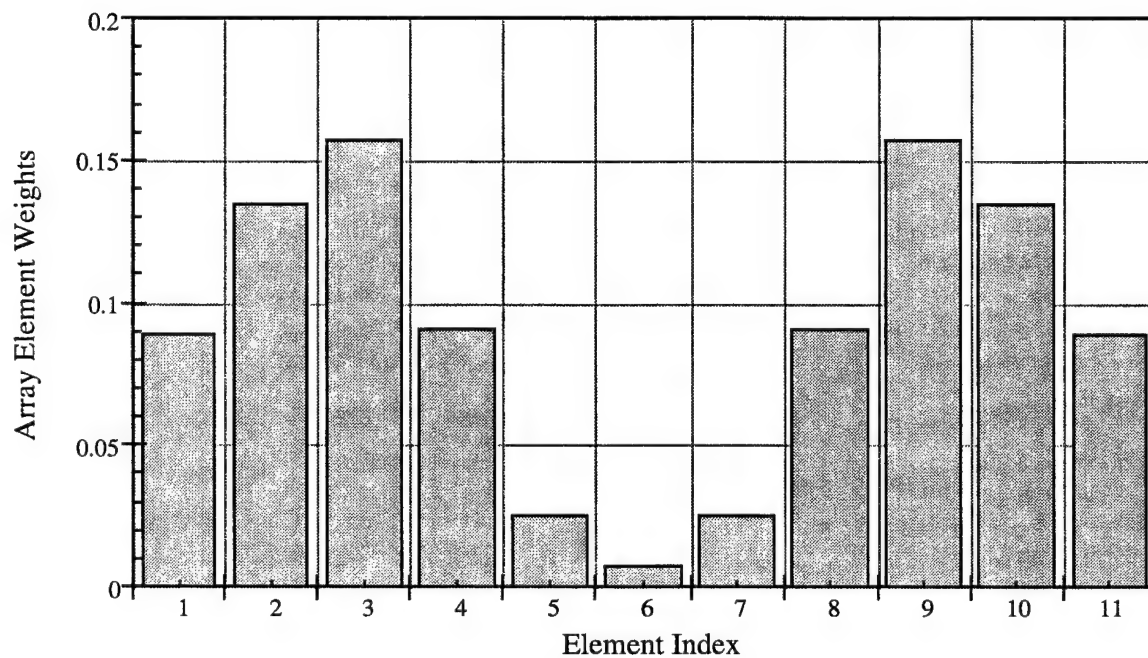
(a) $\theta_l = 180°$
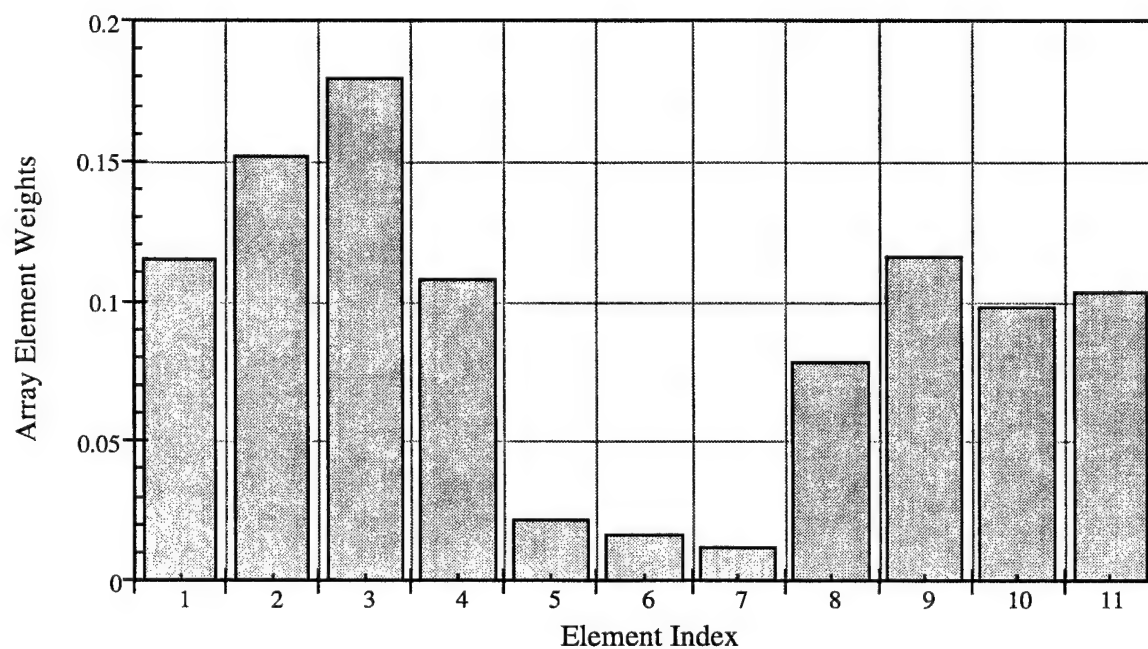
(b) $\theta_l = 150°$

Figure 7. Optimum Weight Distributions for the 11-Element Line Array Described in Figure 6 over the Low-Frequency Band (250 Hz ≤ f ≤ 1000 Hz) for Beam-Steering Angles (a) $\theta_l = 180°$ and (b) $\theta_l = 150°$

17

As previously mentioned, the beamformer optimization applied here is based on the maximization of the deflection coefficient of a square-law detector. Therefore, to describe the array performance, the signal-only angular response (beam pattern) of the array at particular frequencies over the band of interest is not suitable. Instead, the array performance is described in terms of the noise-only beamformer output spectrum $V(f)$. An expression for the noise-only beamformer output spectrum associated with K point-force excitations is given in appendix A in terms of the angular frequency ω and is rewritten in terms of the frequency f in Hertz as

$$V(f; w, \hat{\xi}_l) = \sum_{k=1}^{K} N_k(f) \left| \sum_{m=1}^{M} w_m H(f; p_m, q_k, \hat{\zeta}_k) \exp\left[i \frac{2\pi f}{c} \left(p_m \cdot \hat{\xi}_l \right) \right] \right|^2, \tag{8}$$

where $N_k(f)$ denotes the power spectrum of point source k, p_m is the position vector of hydrophone m, c is the speed of sound, and $H(f; p_m, q_k, \hat{\zeta}_k)$ is the transfer function (spectral Green's function) relating a point force located at q_k and oriented along the $\hat{\zeta}_k$-direction with the response measured at p_m. Note that $(p_m \cdot \hat{\xi}_l)/c$ is the time delay for hydrophone m for a plane wave arrival from direction $\hat{\xi}_l$. The unit vector $\hat{\xi}_l$ in the beam-steering direction is expressed mathematically as

$$\hat{\xi}_l = \hat{x} \sin \theta_l \cos \varphi_l + \hat{y} \sin \theta_l \sin \varphi_l + \hat{z} \cos \theta_l, \tag{9}$$

where $\hat{x}$, $\hat{y}$, and $\hat{z}$ denote unit vectors along the x-, y-, and z-directions, respectively, and θ_l and φ_l denote the polar and azimuthal angles, respectively, of the beam-look direction. (The reader is referred to the coordinate system described in figure 1.) In the examples described in this report, the power spectrum $N_k(f)$ of each noise source is assumed to be unity across the frequency band of interest.

Figures 8a and 8b show plots of the noise-only beamformer output spectra for the line array described in figure 2a as a function of frequency over the low-frequency band for beams steered in the look-directions $\theta_l = 180°$ and $\theta_l = 150°$, respectively. In each of these figures, the beamformer output spectra are plotted for optimum, uniform, and cosine-tapered weights. In each case, the weights sum to unity (i.e., equation (2) is satisfied). For the array in figure 2a, the cosine-tapered weights are given as

$$w_m = b \cos \left[3(\theta_m - \pi) \right], \quad \frac{5\pi}{6} < \theta_m < \frac{7\pi}{6}, \quad m = 1, 2, ..., 11, \tag{10}$$

where the normalization constant b is chosen so that the weights sum to unity. The plots in figures 8a and 8b show that the optimum weights produce a significant improvement in the beamformer output across the entire frequency band of interest. The plots also indicate that the optimum weights result in an improvement of almost two orders of magnitude in the beamformer output spectrum over the uniform and cosine-tapered weights across much of the frequency band plotted. This significant improvement will likewise produce an almost two orders of magnitude improvement in the deflection coefficient. In contrast, the beam patterns for the various weights would not necessarily show an improvement for the optimum weights.

Figures 9a and 9b show plots of the noise-only beamformer output spectra for the line array with three noise sources (as described in figure 6) as a function of frequency over the low-frequency band for beams steered in the look-directions $\theta_l = 180°$ and $\theta_l = 150°$, respectively. The plots indicate a similar improvement in the beamformer output spectrum for the optimum weights over the uniform and cosine-tapered weights. Note that the beamformer output spectrum for each weight distribution is larger than the corresponding one plotted in figures 8a and 8b because there are three times as many noise sources (i.e., $K = 3$ versus $K = 1$ in equation (8)).

As shown by Streit and Wettergren (reference 4), the deflection coefficient d for the beam steered in the look-direction $\hat{\xi}_l$ is inversely proportional to the standard deviation of the square-law detector output waveform under low SNR conditions, i.e.,

$$d \propto \frac{1}{\sqrt{\int_{f_{min}}^{f_{max}} V^2(f; \underline{w}, \hat{\xi}_l) \, df}} \, , \tag{11}$$

where the proportionality constant is the signal power S. In the above expression, note that the integral under the square root is the objective function $F(\underline{w})$ for the optimization problem. For a given weight distribution $\underline{w}$ and beam-steering-direction $\hat{\xi}_l$, the deflection coefficient index d_n is defined as

$$d_n \equiv \frac{S}{\sqrt{\int_{f_{min}}^{f_{max}} V^2(f; \underline{w}, \hat{\xi}_l) \, df}} \, . \tag{12}$$
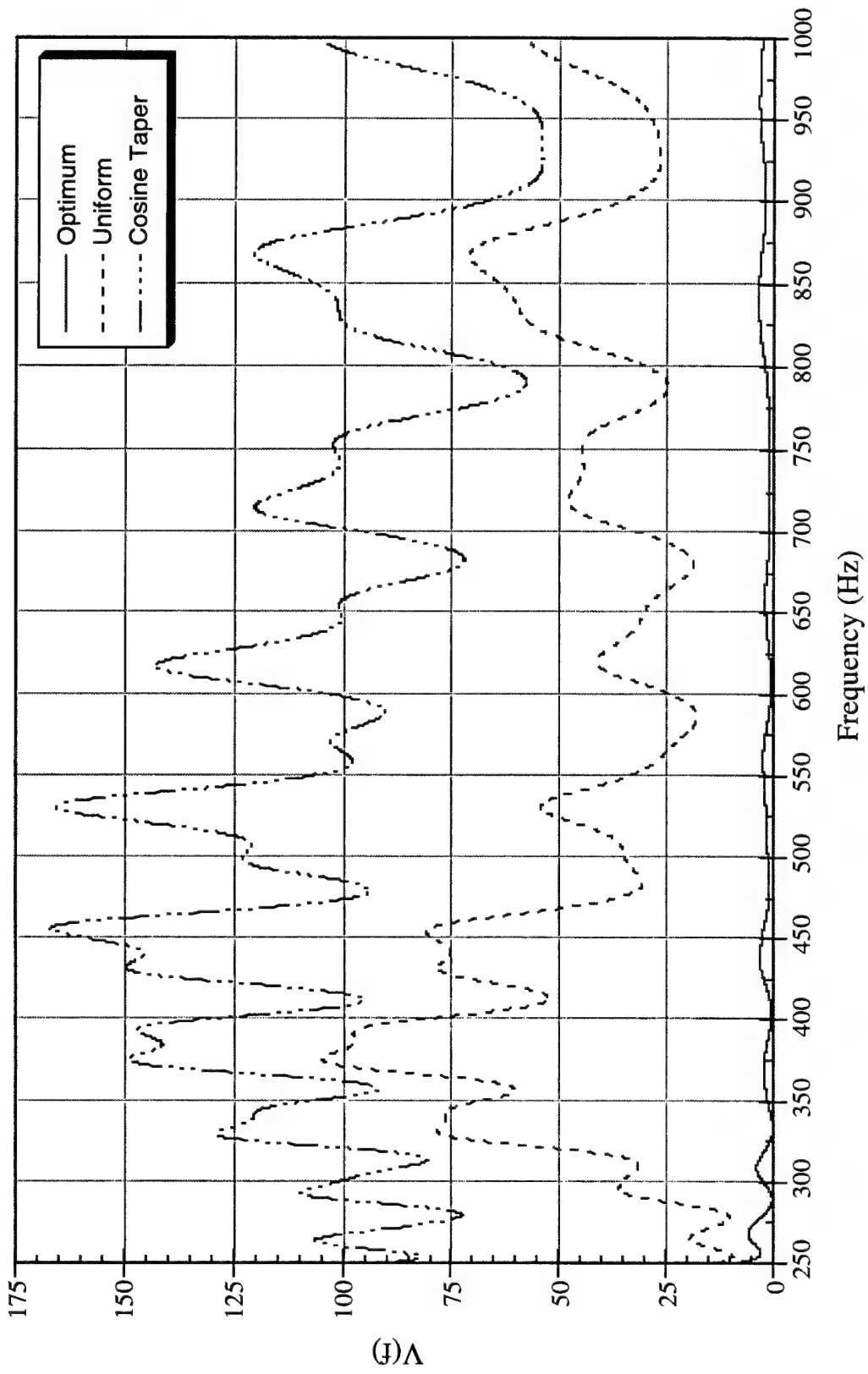
Figure 8a. Noise-Only Beamformer Output Spectra (Low-Frequency Band) for Several Weight Distributions for the Line Array Described in Figure 2a for a Beam Steered at the Look Angle $\theta_l = 180°$

20
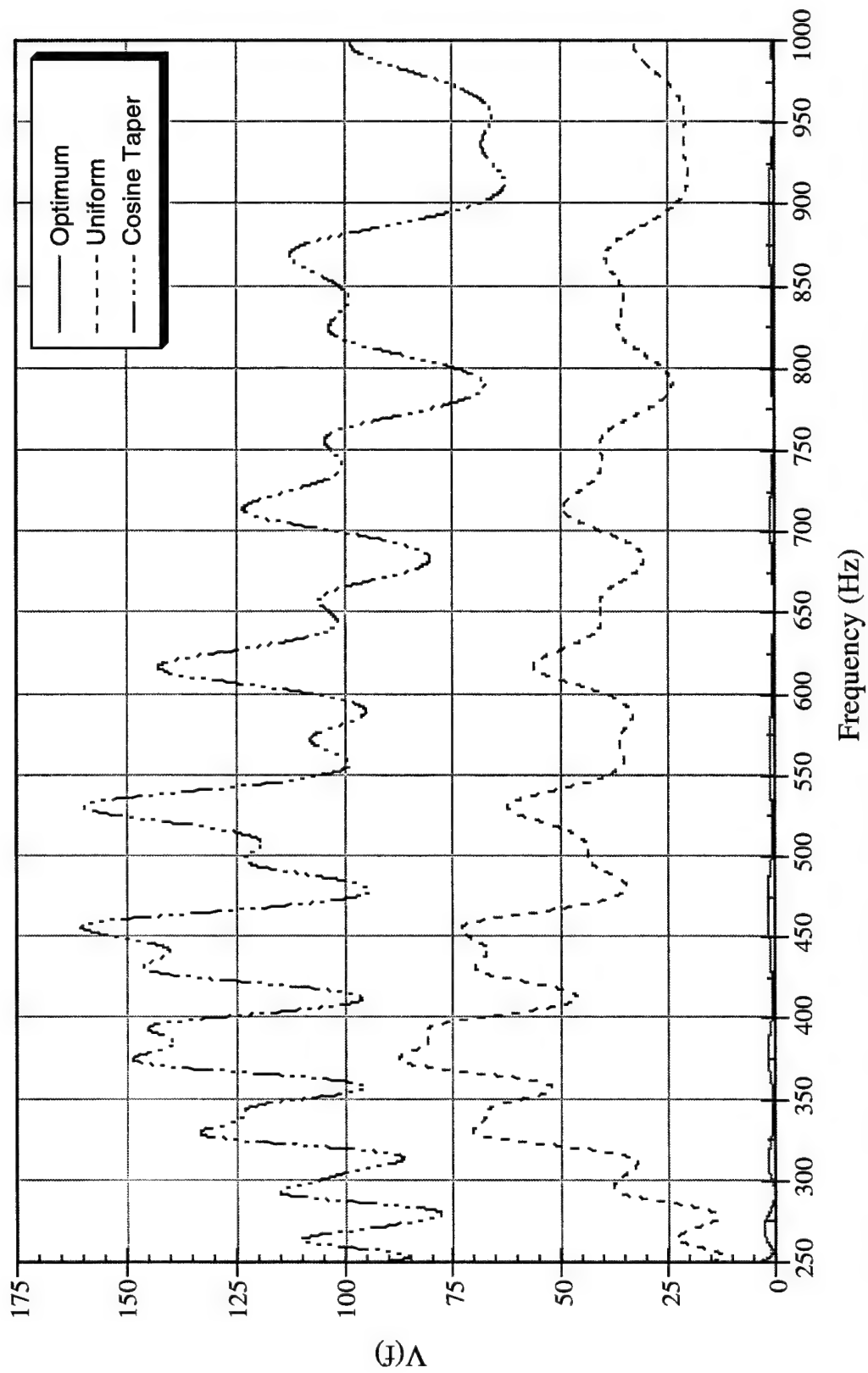
Figure 8b. Noise-Only Beamformer Output Spectra (Low-Frequency Band) for Several Weight Distributions for the Line Array Described in Figure 2a for a Beam Steered at the Look Angle $\theta_l = 150°$

21
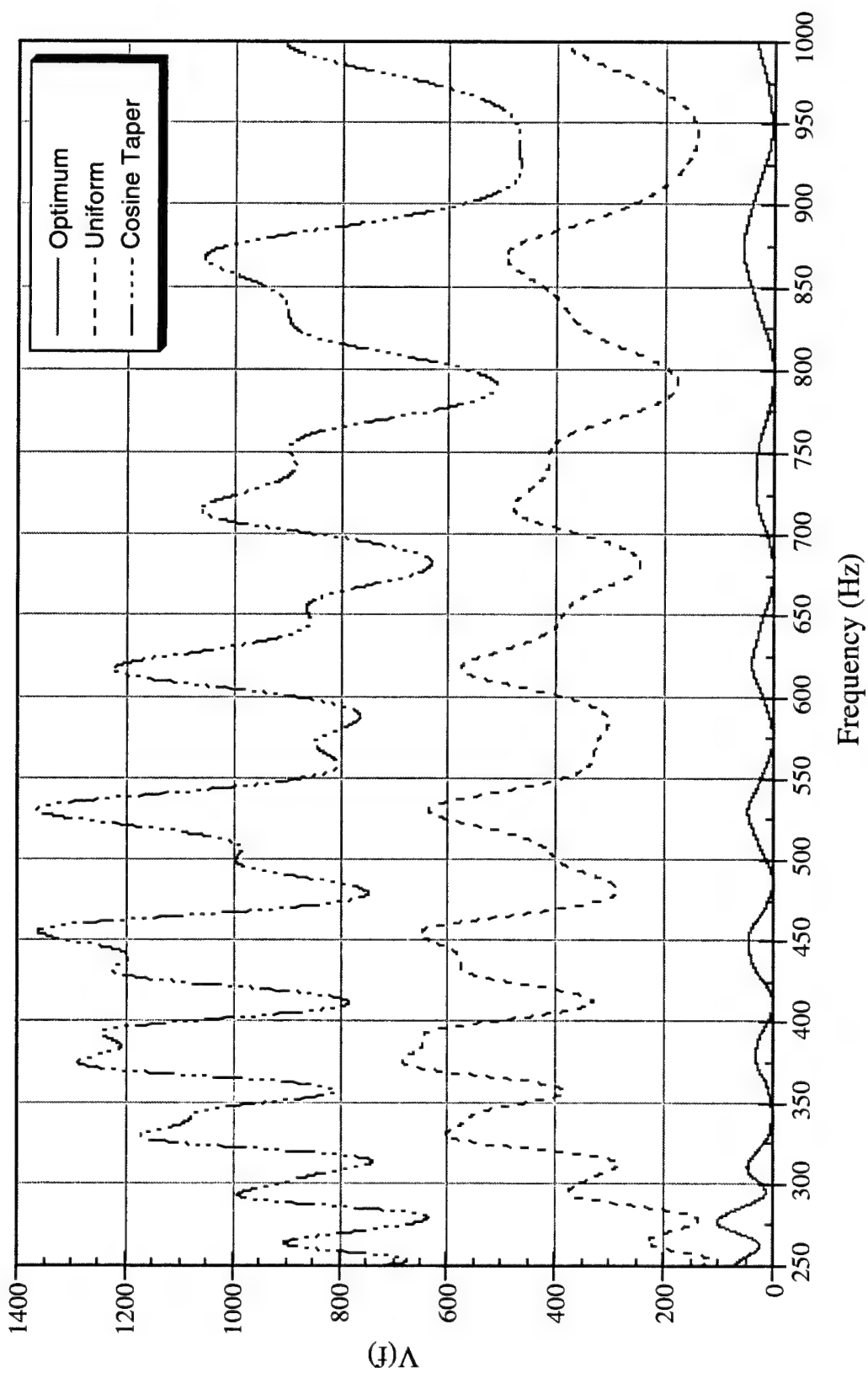
Figure 9a. Noise-Only Beamformer Output Spectra (Low-Frequency Band) for Several Weight Distributions for the Line Array Described in Figure 6 for a Beam Steered at the Look Angle $\theta_l = 180°$

22

Figure 9b. Noise-Only Beamformer Output Spectra (Low-Frequency Band) for Several Weight Distributions for the Line Array Described in Figure 6 for a Beam Steered at the Look Angle $\theta_l = 150°$

23

Because the deflection coefficient is proportional to the SNR at the output of a square-law detector, the difference in deflection coefficient indices for two different weight distributions provides a measure of the difference in the corresponding SNRs at the detector output for a given array. The optimum weight distribution will produce the minimum value for the objective function and will result in the maximum deflection coefficient index.

The SNR improvement with respect to uniform weights ΔSNR_u is defined as

$$\Delta SNR_u \equiv \left. d_n \right|_{opt} - \left. d_n \right|_{unif}, \tag{13}$$

where the subscripts *opt* and *unif* refer to the optimum and uniform weight distributions, respectively. Similarly, the SNR improvement with respect to cosine-tapered weights ΔSNR_c is defined as

$$\Delta SNR_c \equiv \left. d_n \right|_{opt} - \left. d_n \right|_{cos}, \tag{14}$$

where the subscript *cos* refers to the cosine-tapered weight distribution. The SNR improvements above are given in decibels (dB) as

$$\left. \Delta SNR_u \right|_{dB} = 10 \log_{10}(\Delta SNR_u), \tag{15a}$$

and

$$\left. \Delta SNR_c \right|_{dB} = 10 \log_{10}(\Delta SNR_c). \tag{15b}$$

Table 1 presents the objective function for the optimum, uniform, and cosine-tapered weights and the SNR improvements with respect to the uniform and cosine-tapered weights for the low-frequency band examples presented in this report. Particular attention should be made to the first four array examples in the table as these correspond to the results shown in figures 5, 7, 8, and 9. The examples corresponding to the arrays illustrated in figures 2a and 6 show that the optimum weights produce a 22- to 42-dB improvement in the SNR as compared with the conventional uniform and cosine-tapered weight distributions. The significant improvement in the SNR is not surprising considering the beamformer output spectra plots in figures 8 and 9.

24

Table 1. Objective Function F(_w_) for Several Weight Distributions and SNR Improvements (ΔSNR) in the Low-Frequency Band Examples

Array	Beam Steering Angle (deg)	Weight Distribution	Objective Function	ΔSNR (dB)
Figure 2a	180	Optimum	3.536×10^3	-
		Uniform	1.796×10^6	27.1
		Cosine Taper	8.413×10^6	33.8
Figure 2a	150	Optimum	6.008×10^2	-
		Uniform	1.472×10^6	33.9
		Cosine Taper	8.606×10^6	41.6
Figure 6	180	Optimum	6.629×10^5	-
		Uniform	1.207×10^8	22.6
		Cosine Taper	6.141×10^8	29.7
Figure 6	150	Optimum	2.189×10^5	-
		Uniform	1.070×10^8	26.9
		Cosine Taper	5.617×10^8	34.1
Figure 2b	140	Optimum	2.442×10^2	-
		Uniform	8.055×10^3	15.2
		Cosine Taper	4.289×10^2	2.45
Figure 2b	170	Optimum	2.551×10^2	-
		Uniform	6.649×10^3	14.2
		Cosine Taper	4.371×10^2	2.34
Figure 2b*	140	Optimum	5.004×10^2	-
		Uniform	3.575×10^4	18.5
		Cosine Taper	9.025×10^3	12.6

*Denotes removal of elements 8 and 9.

Figure 10a illustrates the optimum element weights for the line array in figure 2b for a beam steered at the look angle $\theta_l = 140°$. The weight distribution is tapered with the maximum weights near the center of the array and the weights dropping off considerably at the ends. A comparison of the weights for elements on opposite sides of the array (with respect to the center element) shows that the larger weights are on the side of the array nearest to the source. Figure 10b shows the optimum weights for the same line array with a beam-steering angle of $\theta_l = 170°$. In this example, the weight distribution is more symmetrical than in figure 10b with a maximum

value at the center element. The optimum distributions in figures 10a and 10b are quite stable as the same results were obtained for several feasible and infeasible starting points.
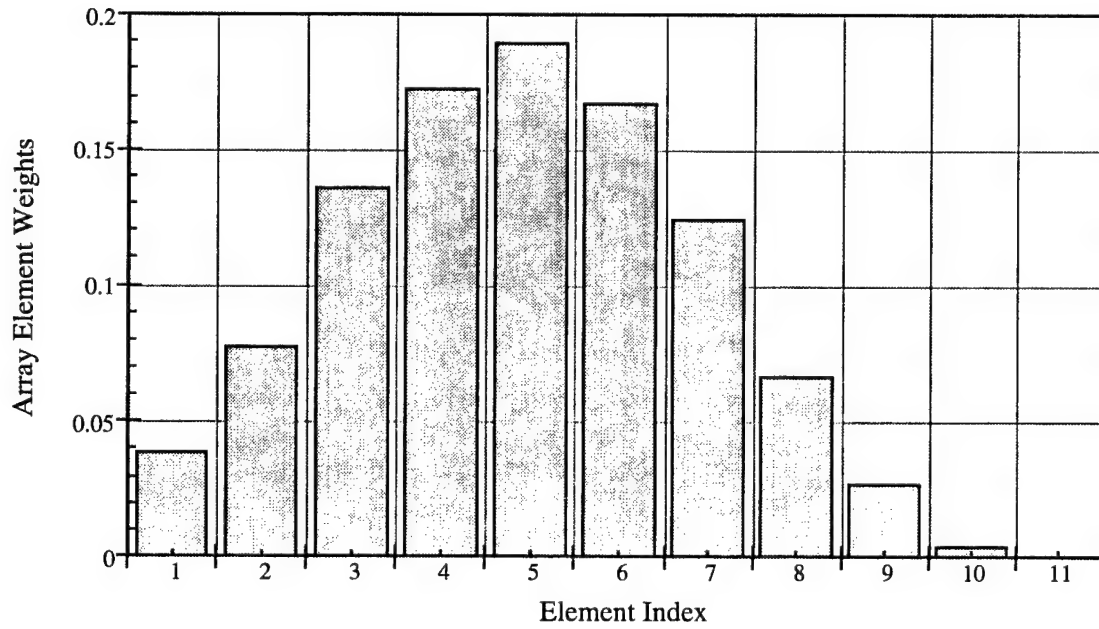
(a) $\theta_l = 140°$
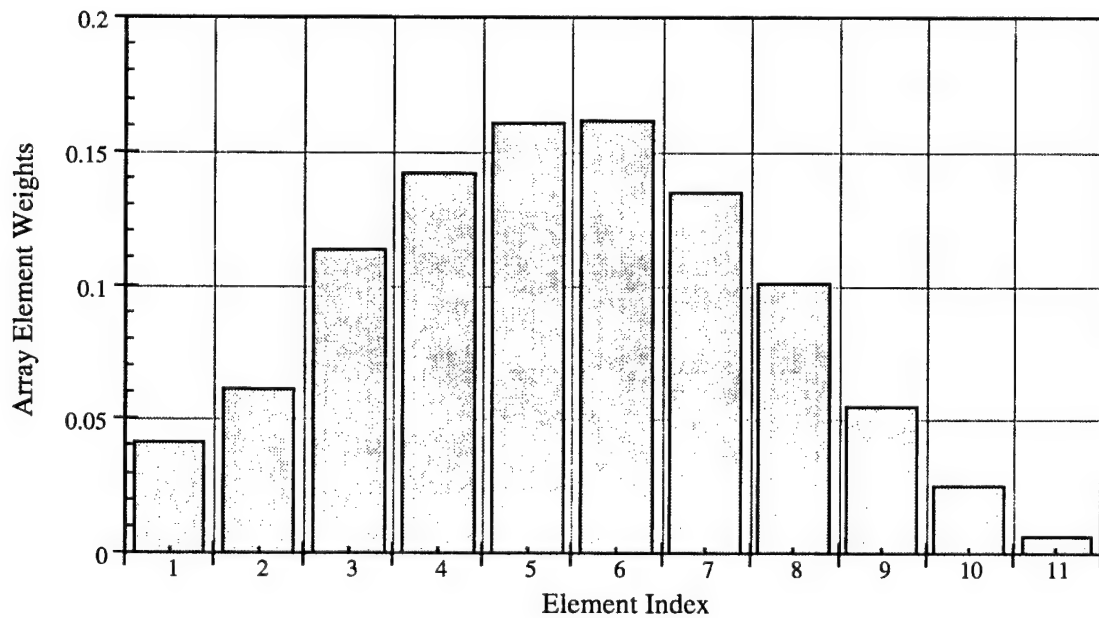
(b) $\theta_l = 170°$

Figure 10. Optimum Weight Distributions for the 11-Element Line Array Described in Figure 2b over the Low-Frequency Band (250 Hz ≤ f ≤ 1000 Hz) for Beam-Steering Angles (a) $\theta_l = 140°$ and (b) $\theta_l = 170°$

Figures 11a and 11b show plots of the noise-only beamformer output spectra for the line array described in figure 2b as a function of frequency over the low-frequency band for beams steered in the look-directions $\theta_l = 140°$ and $\theta_l = 170°$, respectively. As done in the previous examples, the beamformer output spectra are plotted for optimum, uniform, and cosine-tapered weights where the weights sum to unity. For the array in figure 2b, the cosine-tapered weights are given as

$$w_m = b \cos\left[3\left(\theta_m - \frac{7\pi}{9}\right)\right], \quad \frac{11\pi}{18} < \theta_m < \frac{17\pi}{18}, \quad m = 1, 2, ..., 11, \tag{16}$$

where the normalization constant b is chosen so that the weights sum to unity. The plots in figures 11a and 11b show that the optimum weights produce a reduction in the beamformer output spectrum across much of the frequency band of interest. Table 1 shows that the optimum weights produce a SNR improvement between one and two orders of magnitude over the uniform weights. In contrast, figures 11a and 11b show that the cosine-tapered weights produce a beamformer output spectrum that resembles the spectrum produced by the optimum weights. This resemblance is attributed to the optimum weight distributions in figures 10a and 10b being tapered and somewhat symmetric with a maximum at or near the center element. An indication of this close agreement for the cosine-tapered weights is shown in table 1 where the improvement in SNR is only a little more than 2 dB.

Figure 12 is a plot of the optimum weight distribution for the line array in figure 2b with elements 8 and 9 missing and the beam steered at the look angle $\theta_l = 140°$. A comparison of figures 10a and 12 shows that the weights for elements 1 to 5 have increased at the expense of decreased values for the remaining elements. (Although element 10 exists in this example, its weight is zero.) It should be mentioned that the maximum weight in figure 12, w_5, equals 0.207 and exceeds the maximum value allowed in the plot. Figure 13 presents plots of the noise-only beamformer output spectra for the array described in figure 12 for the optimum, uniform, and cosine-tapered weight distributions. The plots show that the optimum weights produce a more noticeable reduction in the beamformer output spectrum than for the array without the missing elements in figure 11a. This observation is validated in table 1, which shows that the optimum weights produce SNR improvements of 18.5 dB and 12.6 dB over the uniform and cosine-tapered distributions, respectively. The increase in SNR improvement with respect to the cosine-tapered weights is attributed to the optimum weight distribution in figure 12 being less tapered and off-centered than the corresponding weight distribution in figure 10a.
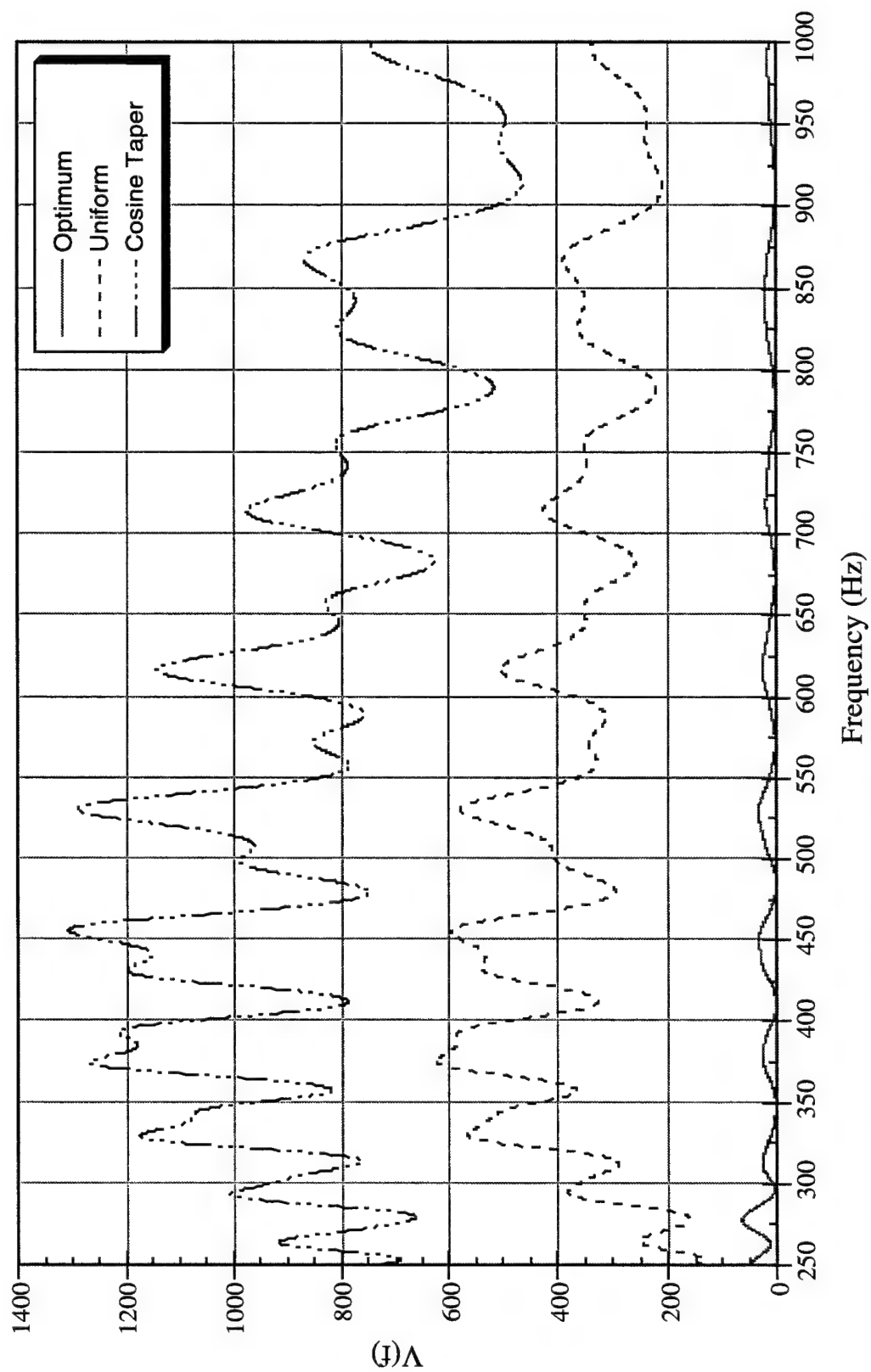
Figure 11a. Noise-Only Beamformer Output Spectra (Low-Frequency Band) for Several Weight Distributions for the Line Array Described in Figure 2b for a Beam Steered at the Look Angle $\theta_l = 140°$

28
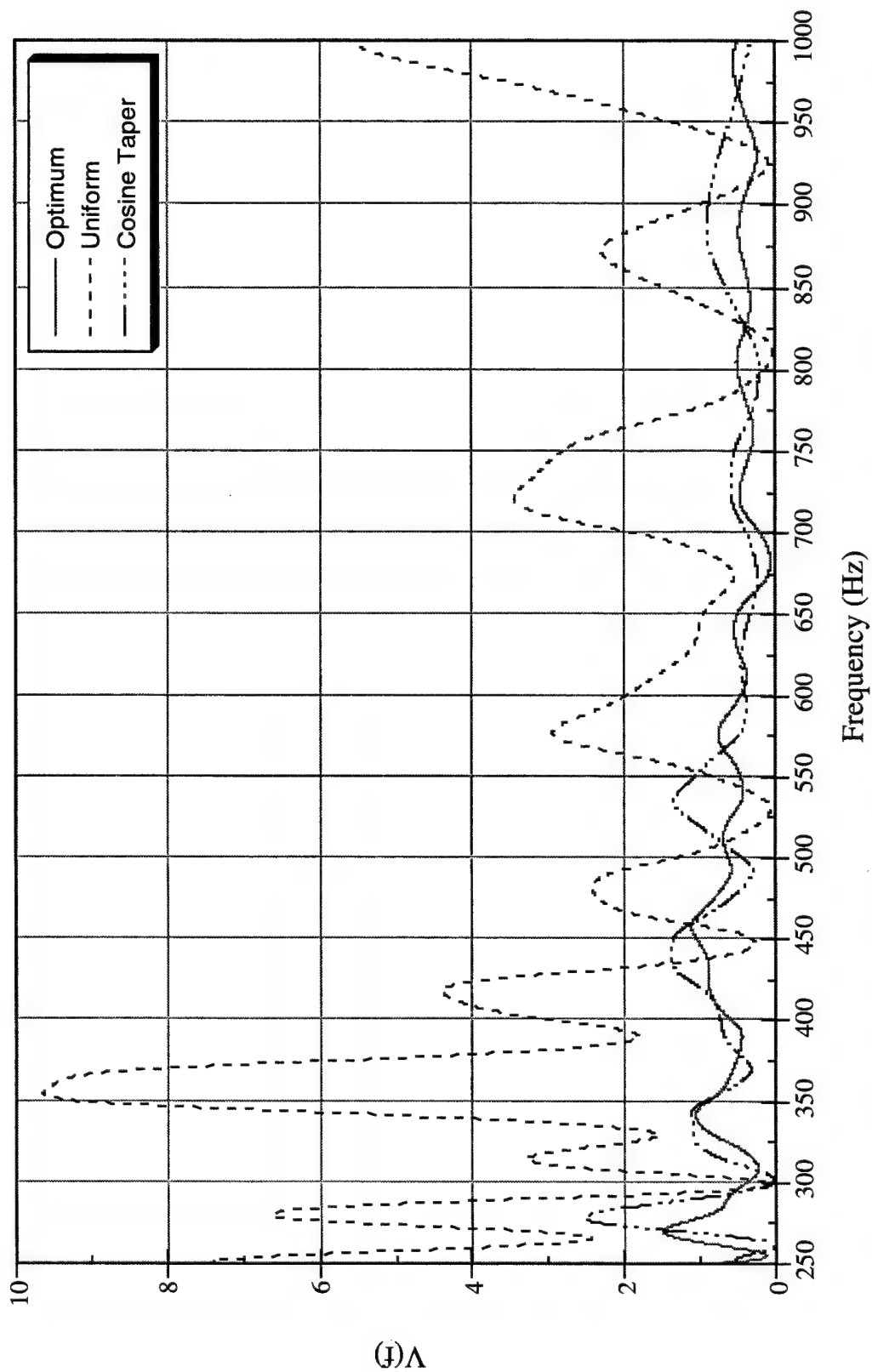
Figure 11b. Noise-Only Beamformer Output Spectra (Low-Frequency Band) for Several Weight Distributions for the Line Array Described in Figure 2b for a Beam Steered at the Look Angle $\theta_l = 170°$

29
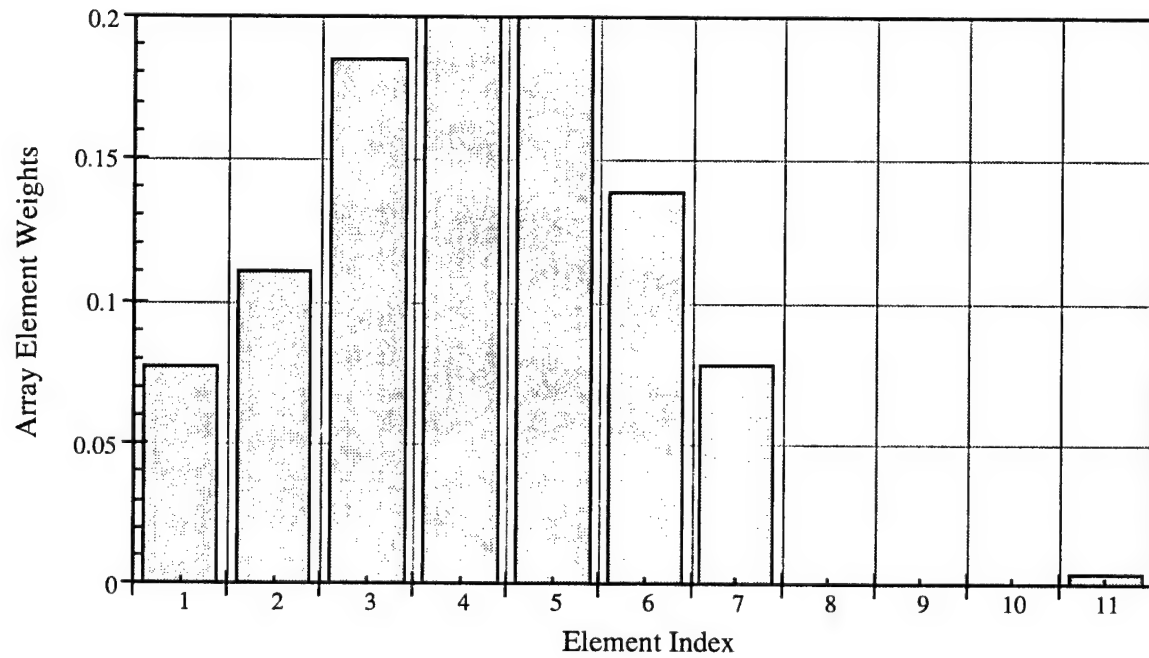
Figure 12. Optimum Weight Distribution for the 11-Element Line Array Described in Figure 2b over the Low-Frequency Band (250 Hz $\leq f \leq$ 1000 Hz) with Elements 8 and 9 Removed (Beam-Steering Angle $\theta_l = 140°$)

30
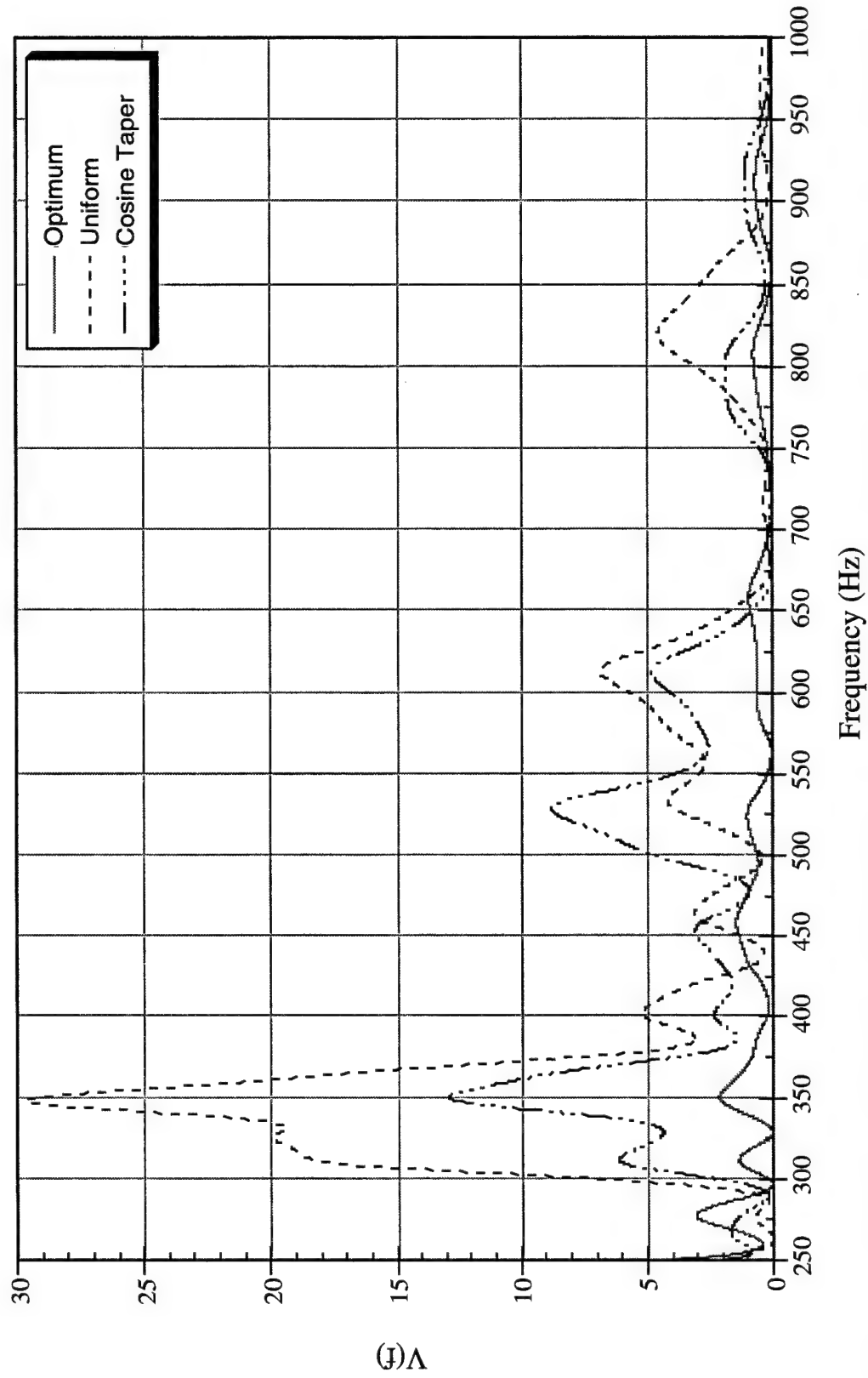
Figure 13. *Noise-Only Beamformer Output Spectra (Low-Frequency Band) for Several Weight Distributions for the Line Array Described in Figure 2b with Elements 8 and 9 Removed and a Beam Steered at the Look Angle $\theta_l = 140°$*

31

4.2 EXAMPLES FOR HIGH-FREQUENCY BAND (1723 Hz $\leq f \leq$ 3446 Hz)

Consider again the 11-element line array centered at $\theta = 180°$ as described in figure 2a. With a time-harmonic point force located at $\theta = 0°$, the resulting transfer function magnitude plots as a function of frequency across the high-frequency band at the locations of elements 1 to 3 and elements 4 to 6 are shown in figures 14a and 14b, respectively. Because the transfer function is axisymmetric for a point source located at $\theta = 0°$, the transfer functions for elements 7 to 11 are not plotted. The plots show that the transfer function at the center element (no. 6) is noticeably larger than at the other element locations over the entire frequency band. (It should be noted that a similar observation was made for the low-frequency band case.)

Figures 15a and 15b are bar graphs of the optimum weight distributions for the line array in figure 2a for beams steered at the look angles $\theta_l = 180°$ and $\theta_l = 150°$, respectively. The optimum weight distribution in figure 15a is somewhat flat, with maxima at elements 5 and 7. In contrast, the weight distribution in figure 15b is irregular, with a maximum at element 11. Comparisons of figures 15a and 15b with their low-frequency counterparts in figures 5a and 5b, respectively, indicate no resemblance.

Figures 16a and 16b are plots of the noise-only beamformer output spectra for the optimum, uniform, and cosine-tapered weights corresponding to the arrays described in figures 15a and 15b, respectively. In each figure, the beamformer output spectrum for the optimum weights is considerably smaller than that for the uniform and cosine-tapered weights. Because the optimum weight distribution in figure 15a is relatively flat, it is no surprise that the beamformer output spectrum for the uniform weights in figure 16a is noticeably smaller than that for the cosine-tapered weights. The graphs in figure 16b show that the beamformer output spectrum for the optimum weight distribution is well below the output spectra for the other weights than in figure 16a. This difference is attributed to the highly irregular optimum weight distribution illustrated in figure 15b.
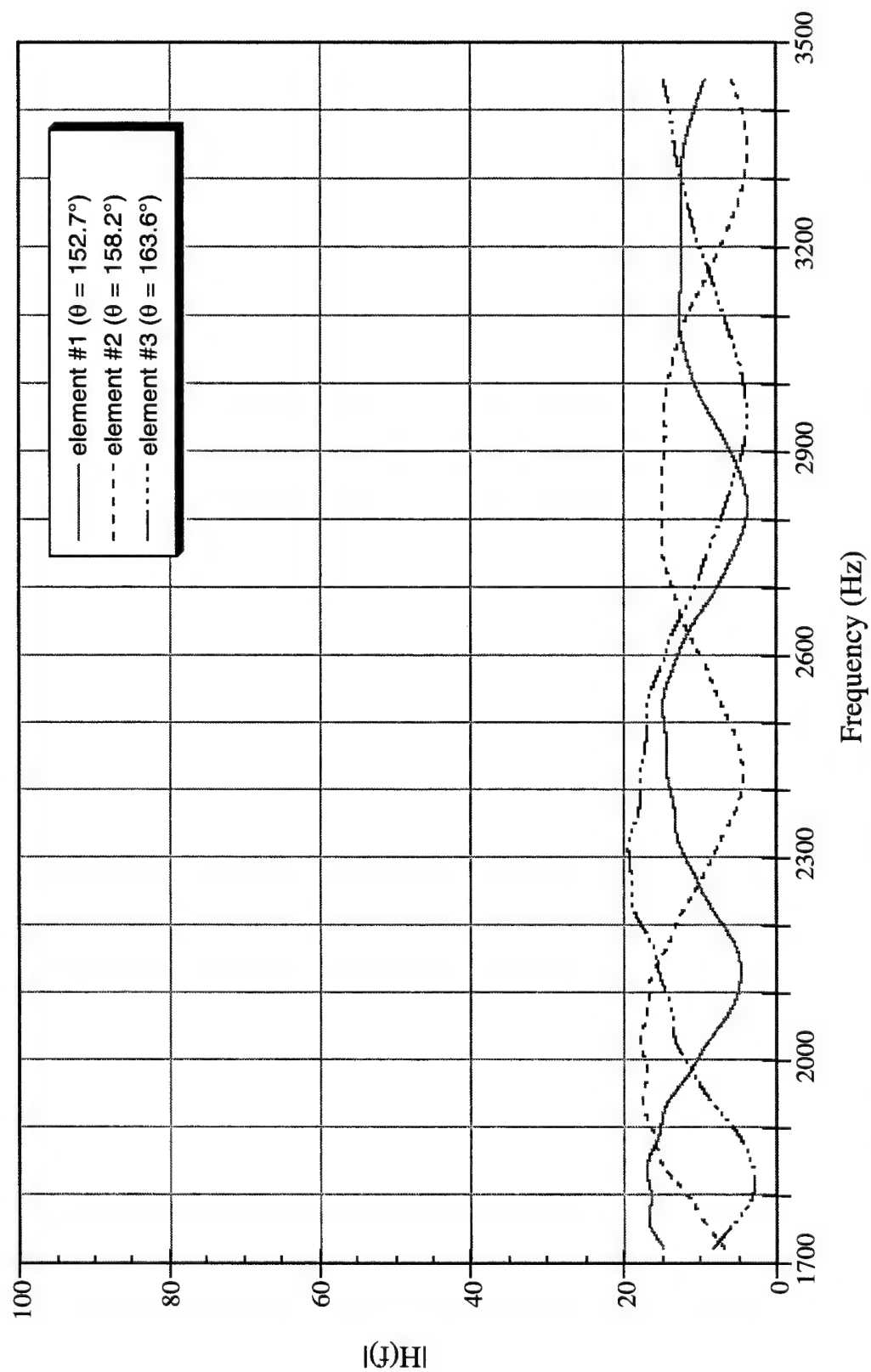
Figure 14a. Transfer Functions over the High-Frequency Band at the Locations of Elements 1 to 3 for the Array Described in Figure 2a

33
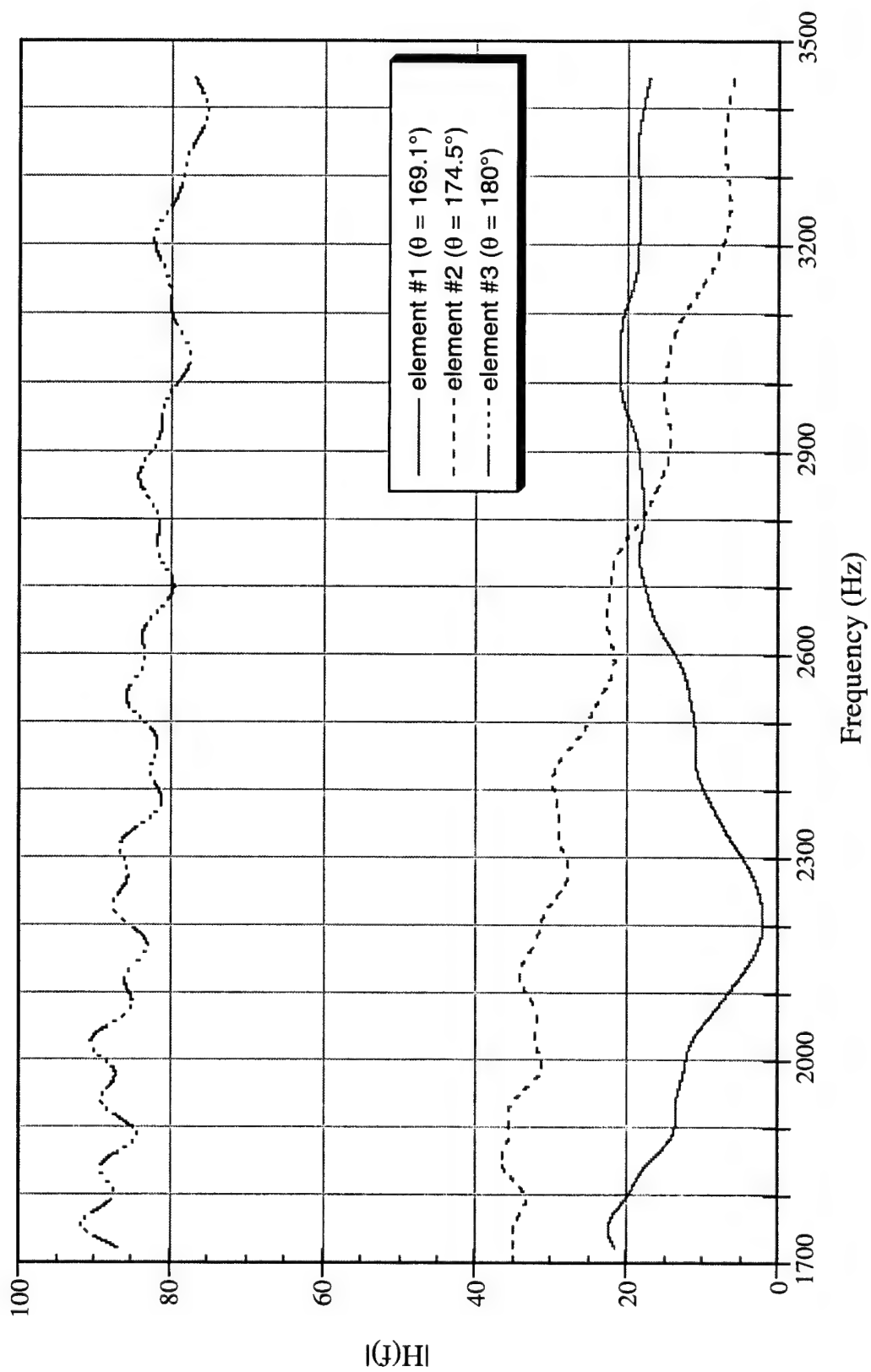
Figure 14b. Transfer Functions over the High-Frequency Band at the Locations of Elements 4 to 6 for the Array Described in Figure 2a
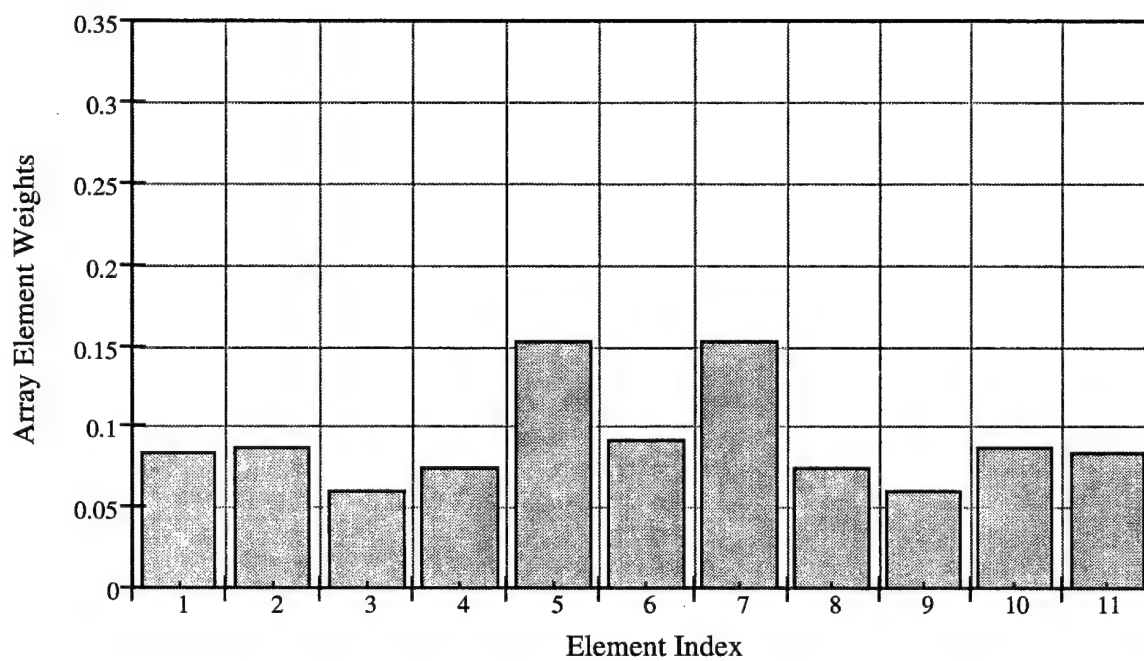
(a) $\theta_l = 180°$
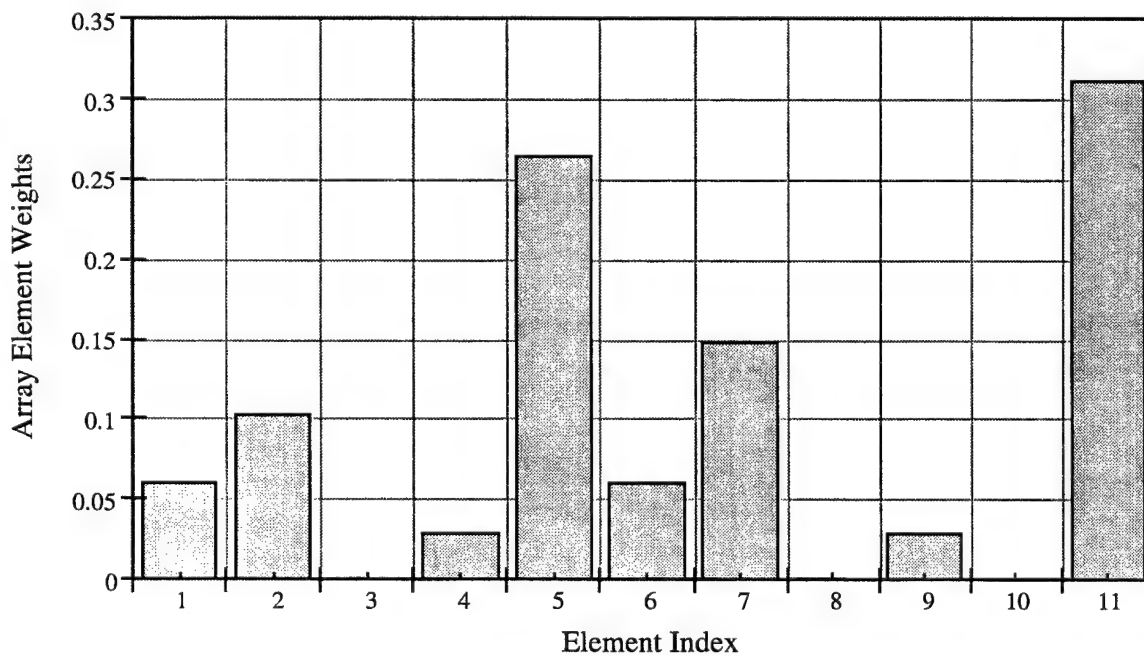
(b) $\theta_l = 150°$

Figure 15. Optimum Weight Distributions for the 11-Element Line Array Described in Figure 2a over the High-Frequency Band (1723 Hz $\leq f \leq$ 3446 Hz) for Beam-Steering Angles (a) $\theta_l = 180°$ and (b) $\theta_l = 150°$

35

Figure 16a. Noise-Only Beamformer Output Spectra (High-Frequency Band) for Several Weight Distributions for the Line Array Described in Figure 2a for a Beam Steered at the Look Angle $\theta_l = 180°$
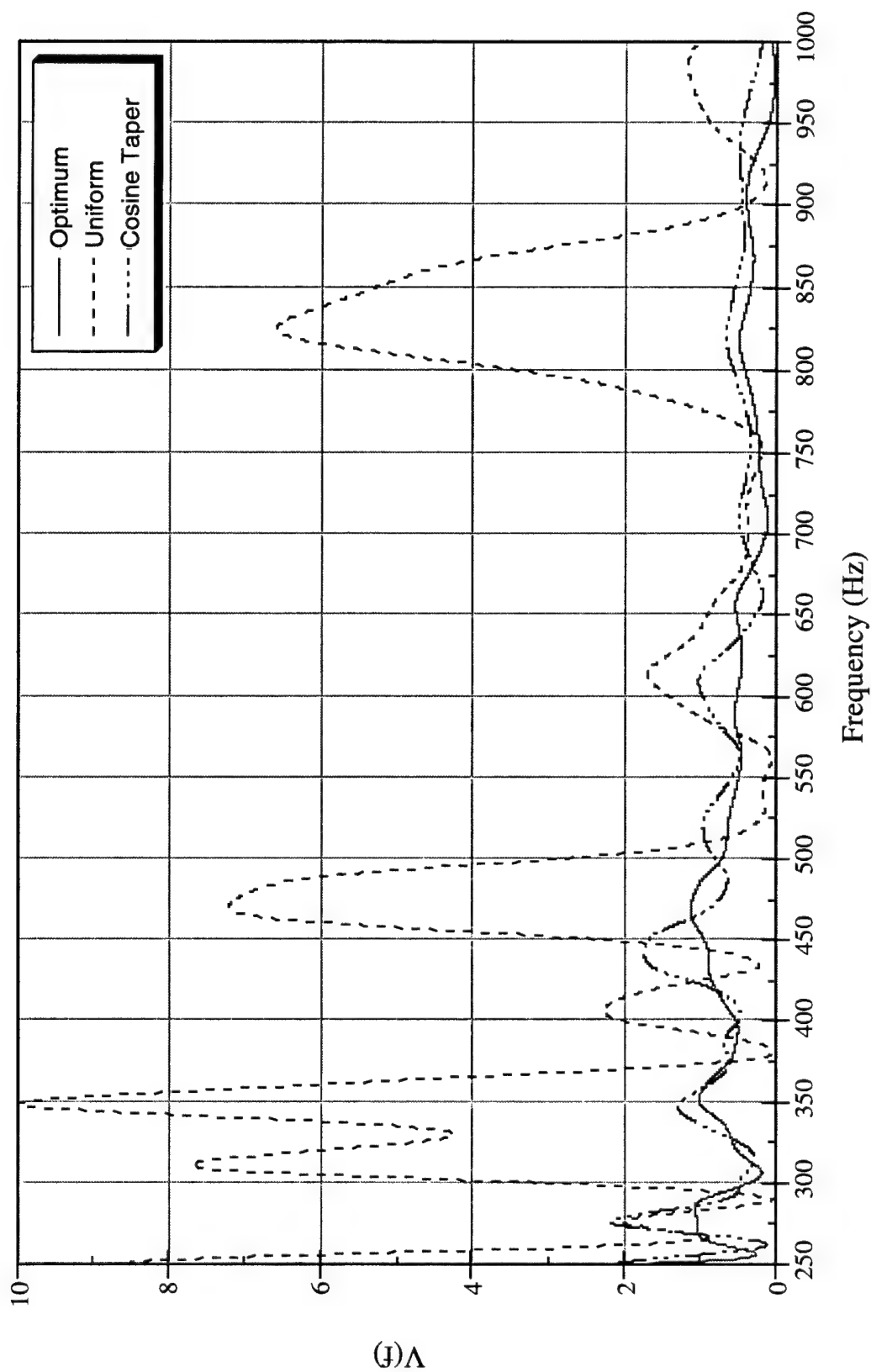
36

Figure 16b. Noise-Only Beamformer Output Spectra (High-Frequency Band) for Several Weight Distributions for the Line Array Described in Figure 2a for a Beam Steered at the Look Angle $\theta_l = 150°$

37

Table 2 gives the objective functions for the optimum, uniform, and cosine-tapered weights and the SNR improvements with respect to the uniform and cosine-tapered weights for the high-frequency band examples presented. The results show that, for the array in figure 2a, the optimum weights produce SNR improvements of 11.5 dB and 17.2 dB over the uniform and cosine-tapered distributions, respectively, when the beam-steering angle is $\theta_l = 180°$. These SNR improvements increase by more than 10 dB when the beam-steering angle is $\theta_l = 150°$. This increase is attributed to the irregular optimum weight distribution shown in figure 15b.

Table 2. Objective Function F(w) for Several Weight Distributions and SNR Improvements (ΔSNR) in the High-Frequency Band Examples

Array	Beam Steering Angle (deg)	Weight Distribution	Objective Function	ΔSNR (dB)
Figure 2a	180	Optimum	3.646×10^4	-
		Uniform	5.112×10^5	11.5
		Cosine Taper	1.935×10^6	17.2
Figure 2a	150	Optimum	3.741×10^4	-
		Uniform	5.793×10^6	21.9
		Cosine Taper	3.578×10^7	29.8
Figure 2b	140	Optimum	2.830×10^3	-
		Uniform	4.006×10^4	11.5
		Cosine Taper	1.991×10^4	8.47
Figure 2b	170	Optimum	9.714×10^3	-
		Uniform	5.535×10^4	7.56
		Cosine Taper	3.270×10^4	5.27

Figures 17a and 17b are bar graphs of the optimum weight distributions for the array described in figure 2b with beam-steering angles of $\theta_l = 140°$ and $\theta_l = 170°$, respectively. The weight distribution in figure 17a is tapered with a maximum value at element 4; the distribution in figure 17b is irregular with a maximum at element 2. Comparison of figures 17a and 17b with the low frequency-bar graphs in figures 10a and 10b indicate that both optimum distributions are tapered when the beam-steering angle is $\theta_l = 140°$, but exhibit no resemblance when $\theta_l = 170°$.

(a) $\theta_l = 140°$
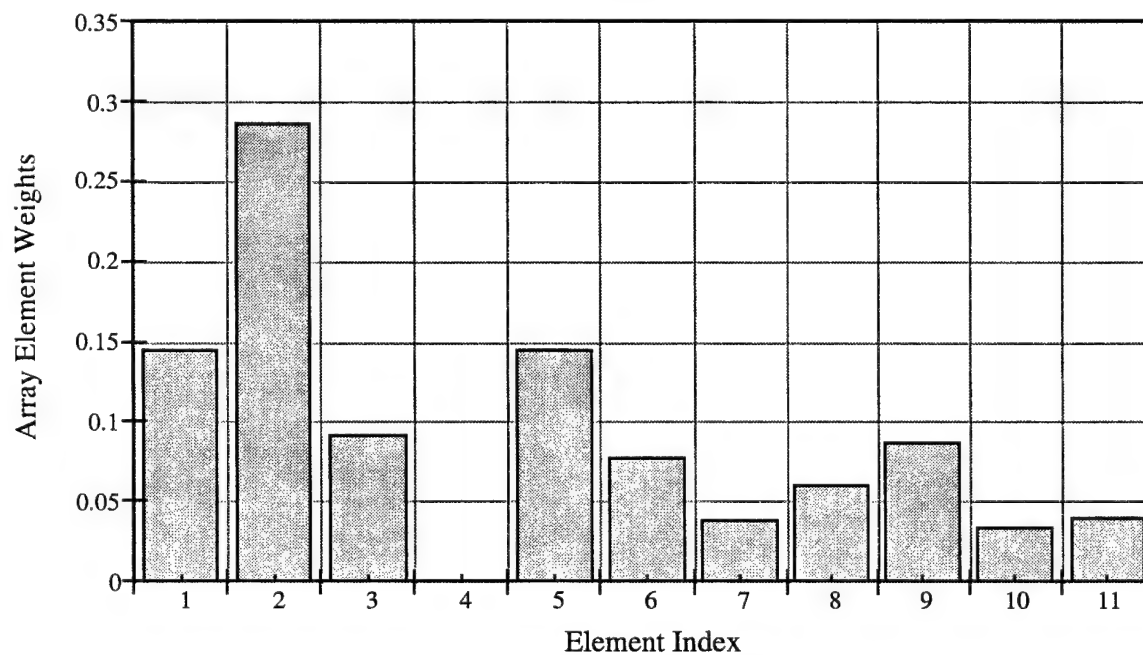
(b) $\theta_l = 170°$

Figure 17. Optimum Weight Distributions for the 11-Element Line Array Described in Figure 2b over the High-Frequency Band (1723 Hz $\leq f \leq$ 3446 Hz) for Beam-Steering Angles (a) $\theta_l = 140°$ and (b) $\theta_l = 170°$

39

Figures 18a and 18b are plots of the noise-only beamformer output spectra for the optimum, uniform, and cosine-tapered weights corresponding to the arrays described in figures 17a and 17b, respectively. As discovered in each of the previous examples, the beamformer output spectrum for the optimum weights is below the spectra for the uniform and cosine-tapered spectra over much of the frequency band of interest. Table 2 shows that for the array depicted in figure 2b the optimum weights produce SNR improvements of 11.5 dB and 8.47 dB over the uniform and cosine-tapered distributions, respectively when the beam-steering angle is $\theta_l = 140°$. The SNR improvements are 3 to 4 dB less when the beam-steering angle is $\theta_l = 170°$.

A comparison of the results listed in tables 1 and 2 gives some indication of the effect of element spacing on the optimization results. The reader should recall that the element spacing s between elements is $0.036\lambda \leq s \leq 0.145\lambda$ over the low-frequency band and $\lambda/4 \leq s \leq \lambda/2$ over the high-frequency band. For the array centered at $\theta = 180°$ (figure 2a), the SNR improvements in the low-frequency band examples are greater than in the corresponding high-frequency band examples. This observation is somewhat surprising considering that the transfer functions at each element location are comparable in magnitude across their respective frequency bands. The expression for the noise-only beamformer output spectrum $V(f)$ in equation (8) indicates that the differences in these results are most likely attributed to phase differences in the element transfer functions and in the exponential term in equation (8). For the array centered at $\theta = 140°$ (figure 2b), the SNR improvements, with respect to uniform weights, are greater in the low-frequency band examples. However, the high-frequency band examples produce larger SNR improvements with respect to cosine-tapered weights.
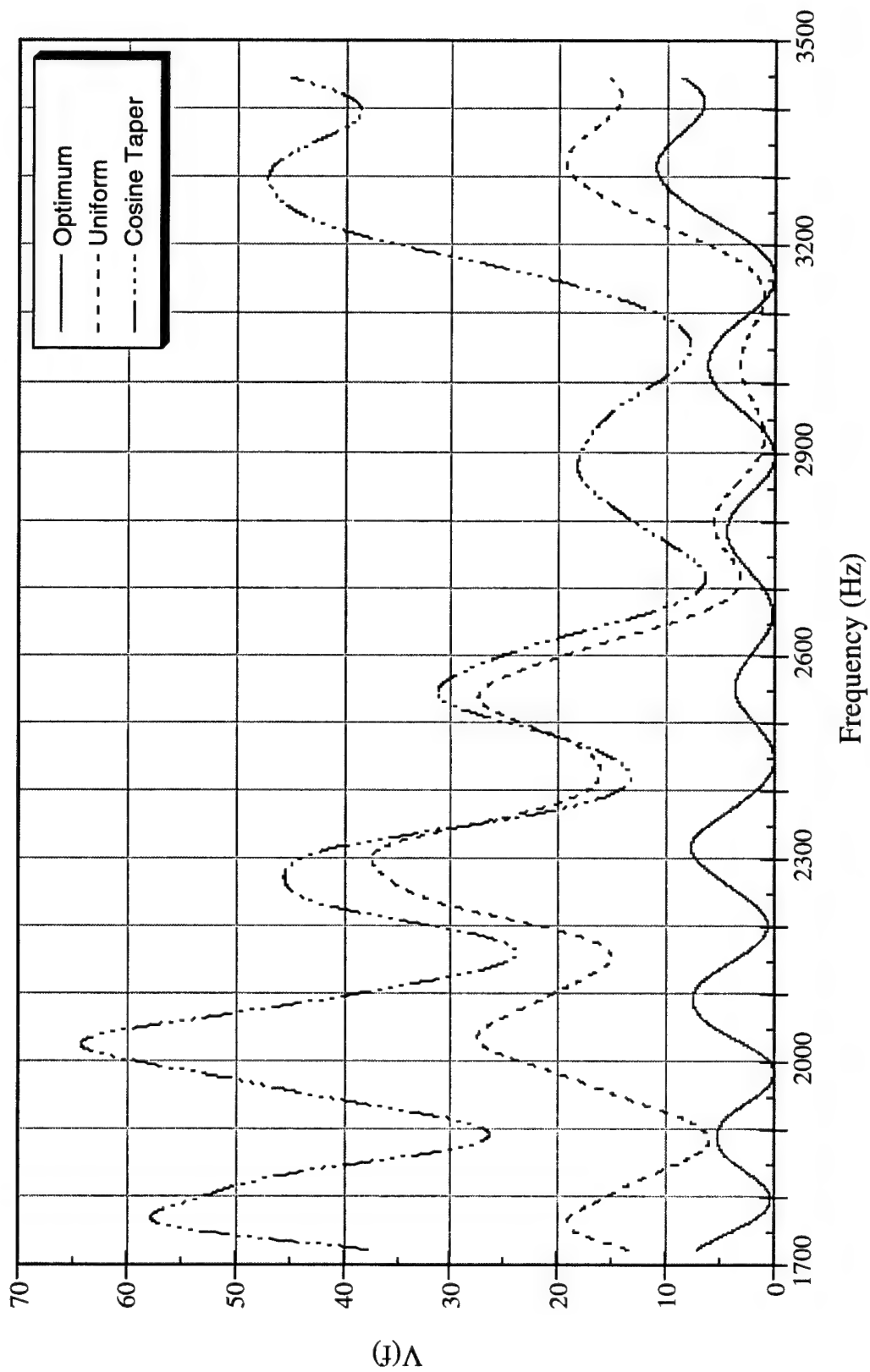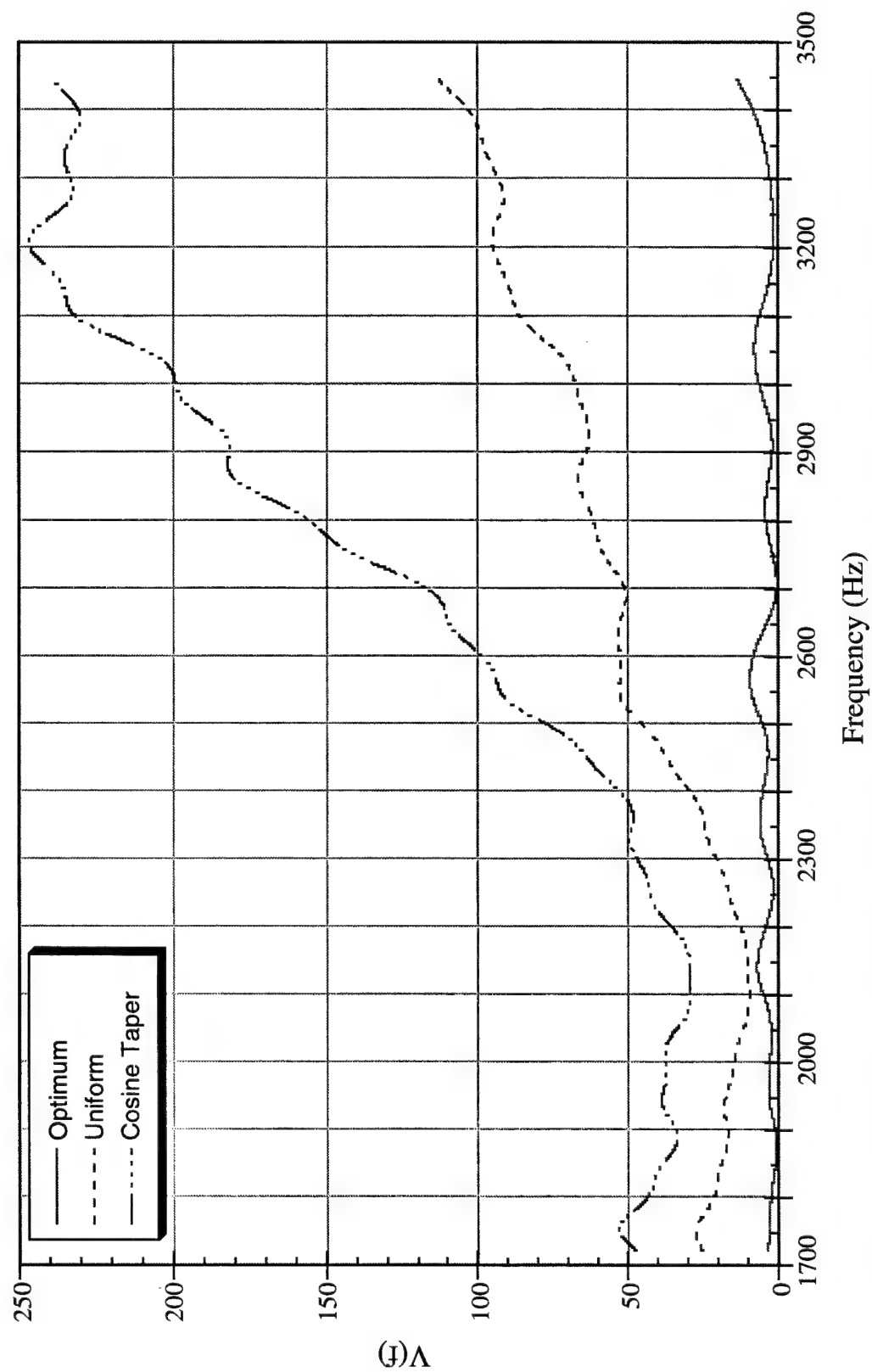
40
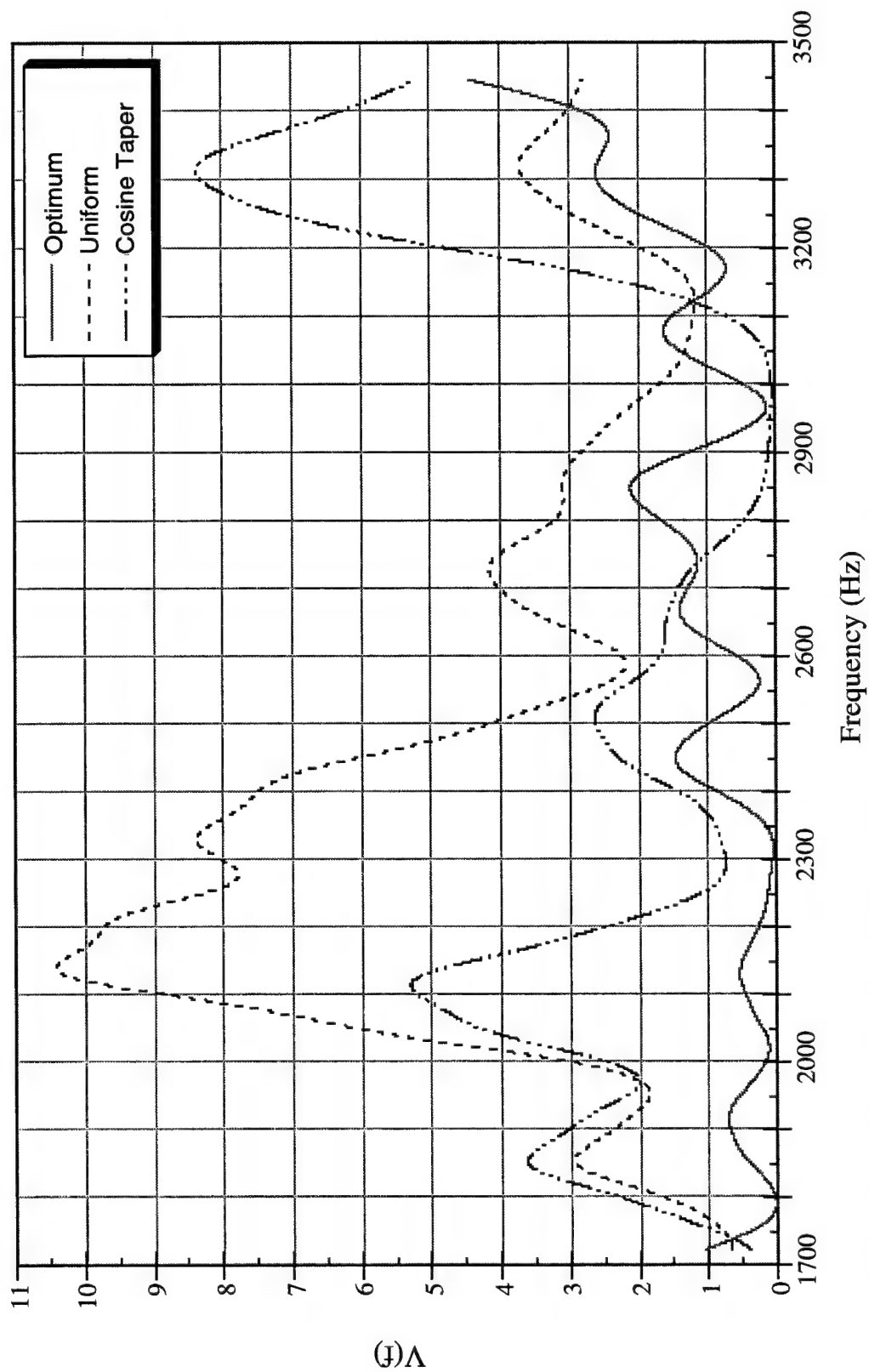
Figure 18a. Noise-Only Beamformer Output Spectra (High-Frequency Band) for Several Weight Distributions for the Line Array Described in Figure 2b for a Beam Steered at the Look Angle $\theta_l = 140°$
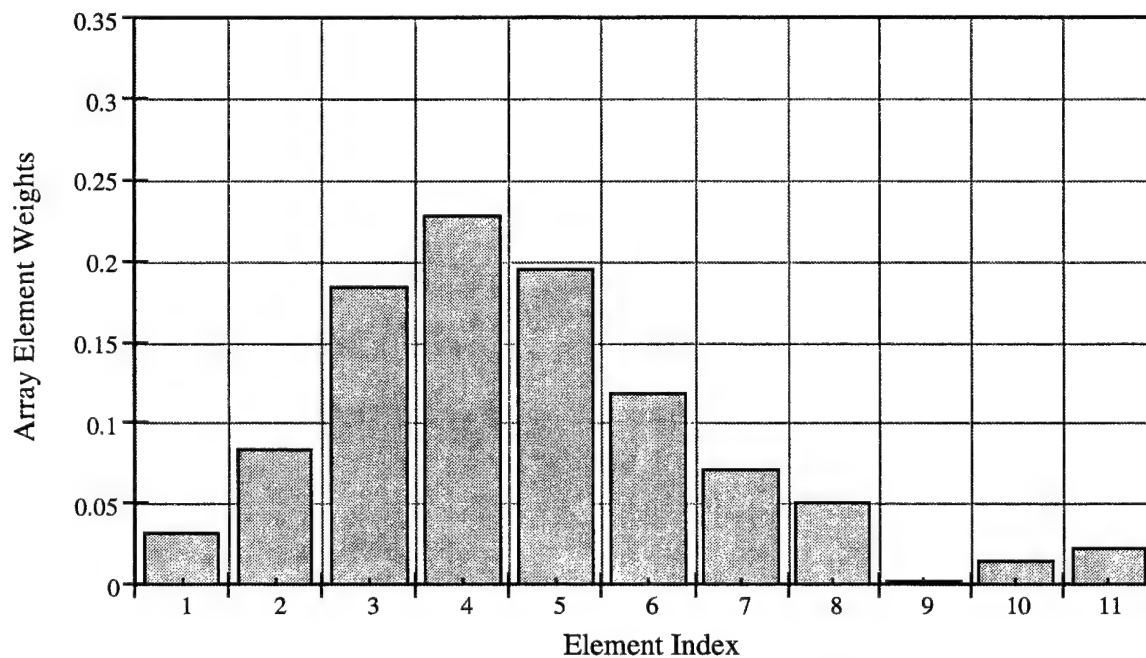
41
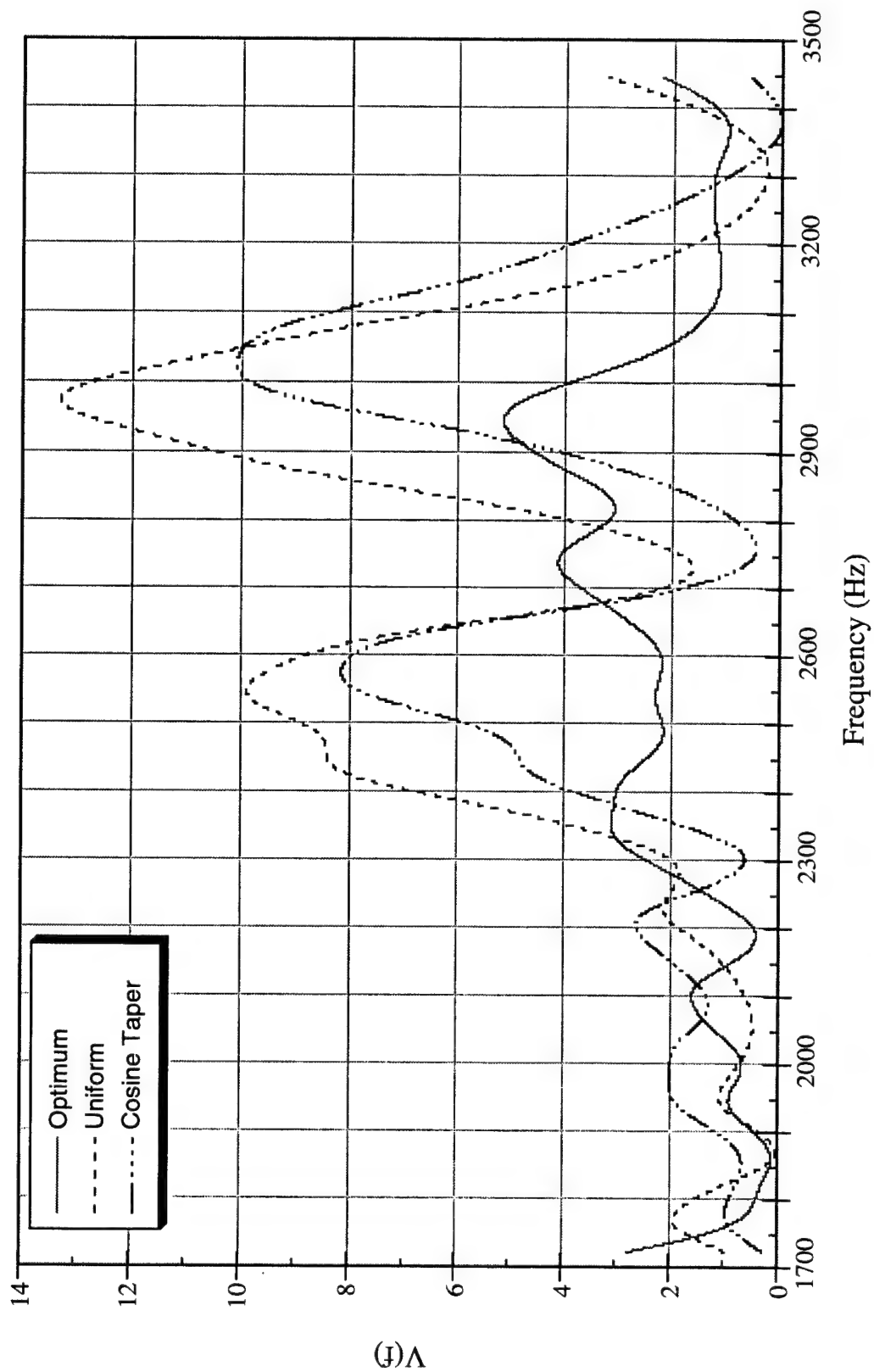
Figure 18b. Noise-Only Beamformer Output Spectra (High-Frequency Band) for Several Weight Distributions for the Line Array Described in Figure 2b for a Beam Steered at the Look Angle $\theta_l = 170°$

42

5. CONCLUSIONS

The results presented in this report have shown that the optimal broadband array design procedure developed by Streit and Wettergren produces a significant improvement in the SNR at the output of a square-law detector when compared with several conventional array weight distributions. These results indicate that this approach shows considerable promise in future submarine acoustic hull array design. In order to apply the optimal broadband array design procedure, the power spectra of the noise sources must be known at a sufficient number of discrete frequencies across the band of interest. These discrete frequencies do not need to be equally spaced. In the examples presented here, the noise spectra are assumed to be flat across the frequency band of interest. The noise power spectra can be obtained either from measurements or from a structural acoustic analysis of a submarine hull.

Each of the examples presented in this report involved an 11-element line array lying along the surface of a 15-ft-diameter, air-filled, fluid-loaded spherical shell. The spherical geometry permitted the application of analytical formulas for the transfer functions that relate a point-force excitation at one point on the sphere to the resulting surface pressure observed by a hydrophone at another point on the sphere. The computation times required to generate the optimization results presented in these examples were generally no more than 30 s on the NUWC Silicon Graphics Onyx 2 Computer. The computation times are expected to increase as a result of the following: (1) the number of array elements increase; (2) the number of discrete noise sources increase; (3) the discrete sources are replaced by continuous ones.

In the upcoming applications planned for the optimal broadband array design procedure, the air-filled, fluid-loaded spherical shell will be replaced by a larger sphere that is fluid filled. This example will help to simulate an array conformal to a submarine sonar dome. In addition, examples involving a continuous noise source and several closely spaced line arrays are planned.

APPENDIX A
DEVELOPMENT OF THE OBJECTIVE FUNCTION AND ITS GRADIENT FOR USE IN THE OPTIMIZATION ALGORITHM

The objective function and corresponding gradient for the optimum hull array design have been derived by Streit and Wettergren (reference 4). In this appendix, the objective function and corresponding gradient of Streit and Wettergren are revised for use in the optimization algorithm.

Consider $K \geq 1$ point-force excitations

$$\alpha_1(t; \boldsymbol{q}_1, \hat{\xi}_1), \ \alpha_2(t; \boldsymbol{q}_2, \hat{\xi}_2), \ ..., \ \alpha_k(t; \boldsymbol{q}_k, \hat{\xi}_k)$$

at hull locations specified by the position vectors $\boldsymbol{q}_1, \boldsymbol{q}_2, ... \boldsymbol{q}_k$, oriented along the directions specified by the unit vectors $\hat{\xi}_1, \hat{\xi}_2, ..., \hat{\xi}_k$ and with power spectra $N_1(\omega), N_2(\omega), ..., N_K(\omega)$, respectively. If the excitations are statistically independent, then the beamformer output spectrum is given by

$$V_o(\omega; \underline{w}, \hat{\xi}_l) = \sum_{k=1}^{K} N_k(\omega) \left| \sum_{m=1}^{M} w_m H(-i\omega; \boldsymbol{p}_m, \boldsymbol{q}_k, \hat{\xi}_k) \exp\left[i\omega \frac{(\boldsymbol{p}_m \cdot \hat{\xi}_l)}{c}\right] \right|^2, \qquad \text{(A-1)}$$

where ω is the angular frequency, $\underline{w} = [w_1, w_2, ..., w_M]^T$ is the column vector of element weights, $\boldsymbol{p}_m$ is the position vector of element m, c is the speed of sound, $\hat{\xi}_l$ is the unit vector in the beam look direction, and $H(-i\omega, \boldsymbol{p}_m, \boldsymbol{q}_k, \hat{\xi}_k)$ is the transfer function (spectral Green's function) relating a point force located at $\boldsymbol{q}_k$ and oriented along the $\hat{\xi}_k$-direction with the response measured at $\boldsymbol{p}_m$. Note that $(\boldsymbol{p}_m \cdot \hat{\xi}_l)/c$ is the time delay for hydrophone m for a plane wave arrival from direction $\hat{\xi}_l$.

Consider a hull array that is designed to maximize the deflection coefficient for the beam steered in the look direction $\hat{\xi}_l$. In this case, the only array design parameters are the element weights $\underline{w}$. Under the assumptions that (1) $\hat{\xi}_l$ is exactly the signal arrival direction, (2) the acoustic signal excites only the hydrophones and not the hull, and (3) the individual hydrophone acoustic beam patterns are omnidirectional with flat spectral response, Streit and Wettergren (reference 4) have shown that the optimum deflection coefficient is found by solving the following minimization problem:

$$\min_{\underline{w} \in R^M} F_o(\underline{w}) = \min_{\underline{w} \in R^M} \int_{-B}^{B} V_o^2(\omega; \underline{w}, \hat{\underline{\xi}}_l) \, d\omega, \tag{A-2}$$

subject to the linear equality constraint

$$\sum_{m=1}^{M} w_m = 1, \tag{A-3}$$

and the non-negative constraint on the hydrophone weights

$$w_m \geq 0, \quad m = 1, 2, ..., M. \tag{A-4}$$

In equation (A-2), V_o is the beamformer output given in equation (A-1) and B denotes the specified array bandwidth.

To obtain optimization results for the problem described in equations (A-2) to (A-4), some simplification of the objective function $F_o(\underline{w})$ is required. Because the autocorrelation functions of the K-excitation waveforms and corresponding beamformer outputs are real and even functions of time, the beamformer output spectrum is a real and even function of ω (reference 13). In addition, it is more convenient to convert from the angular frequency ω to the frequency f in Hertz through the relation $f = \omega/2\pi$. With the substitution of the above into equation (A-2), the objective function simplifies to

$$\tilde{F}(\underline{w}) = 4\pi \int_{0}^{f_{max}} V^2(f; \underline{w}, \hat{\underline{\xi}}_l) \, df, \tag{A-5}$$

where $f_{max} = B/2\pi$, and the beamformer output spectrum V is equivalent to V_o in equation (A-1) with ω replaced by $2\pi f$. Because the array processor also includes a filter that removes the lowest frequencies over the band $0 \leq f < f_{min}$, the limits of integration in equation (A-5) extend over the interval (f_{min}, f_{max}). The factor of 4π in the objective function has no effect on the determination of the optimum array weights. Thus, equation (A-5) reduces to

$$F(\underline{w}) = \int_{f_{min}}^{f_{max}} V^2(f; \underline{w}, \hat{\underline{\xi}}_l) \, df. \tag{A-6}$$

Therefore, the single-beam design optimization problem is

A-2

$$\min_{\underline{w} \in R^M} F(\underline{w}), \tag{A-7}$$

with constraints given by equations (A-3) and (A-4), where the objective function $F(\underline{w})$ is given by equation (A-6). It should be noted that the optimization problem as described by equation (A-7) with equations (A-3) and (A-4) is equivalent to the original optimization problem as described by equation (A-2) with (A-3) and (A-4).

The computation of the gradient of the objective function and its constraints are necessary in the determination of the optimum array weights $\underline{w}$. The gradient of the objective function in equation (A-6) with respect to the array weights is given by

$$\nabla_{\underline{w}} F(\underline{w}) = \int_{f_{\min}}^{f_{\max}} \nabla_{\underline{w}} \left[V^2(f; \underline{w}, \hat{\xi}_l) \right] df = 2 \int_{f_{\min}}^{f_{\max}} V(f; \underline{w}, \hat{\xi}_l) \, \nabla_{\underline{w}} V(f; \underline{w}, \hat{\xi}_l) \, df, \tag{A-8}$$

where the gradient operator $\nabla_{\underline{w}}$ is defined by

$$\nabla_{\underline{w}} = \left[\frac{\partial}{\partial w_1}, \frac{\partial}{\partial w_2}, \ldots, \frac{\partial}{\partial w_M} \right]^T. \tag{A-9}$$

For convenience, the following complex-valued auxiliary function is defined as

$$\varphi(f; \underline{w}, \hat{\xi}, q, \hat{\zeta}) = \sum_{m=1}^{M} w_m \, H(f; p_m, q, \zeta) \, \exp\left[i \frac{2\pi f}{C} \left(p_m \cdot \hat{\xi} \right) \right]. \tag{A-10}$$

The beamformer output spectrum V given in equation (A-1) with ω replaced by $2\pi f$ can be expressed in terms of the auxiliary function φ as

$$V(f; \underline{w}, \hat{\xi}_l) = \sum_{k=1}^{K} N_k(f) \left| \varphi(f; \underline{w}, \hat{\xi}_l, q_k, \hat{\zeta}_k) \right|^2$$

$$= \sum_{k=1}^{K} N_k(f) \, \varphi(f; \underline{w}, \hat{\xi}_l, q_k, \hat{\zeta}_k) \, \varphi^*(f; \underline{w}, \hat{\xi}_l, q_k, \hat{\zeta}_k), \tag{A-11}$$

where * denotes the complex conjugate. Therefore, the gradient of the beamformer output spectrum is

$$\nabla_{\underline{w}} V(f; \underline{w}, \hat{\xi}_l) = \sum_{k=1}^{K} N_k(f) \nabla_{\underline{w}} \left[\varphi(f; \underline{w}, \hat{\xi}_l, \boldsymbol{q}_k, \hat{\zeta}_k) \varphi^*(f; \underline{w}, \hat{\xi}_l, \boldsymbol{q}_k, \hat{\zeta}_k) \right]$$

$$= 2 \sum_{k=1}^{K} N_k(f) \operatorname{Re} \left\{ \varphi(f; \underline{w}, \hat{\xi}_l, \boldsymbol{q}_k, \hat{\zeta}_k) \nabla_{\underline{w}} \left[\varphi^*(f; \underline{w}, \hat{\xi}_l, \boldsymbol{q}_k, \hat{\zeta}_k) \right] \right\}. \quad \text{(A-12)}$$

The nth component of the gradient of V is

$$\frac{\partial V(f; \underline{w}, \hat{\xi}_l)}{\partial w_n} = 2 \sum_{k=1}^{K} N_k(f) \operatorname{Re} \left\{ \varphi(f; \underline{w}, \hat{\xi}_l, \boldsymbol{q}_k, \hat{\zeta}_k) \frac{\partial \varphi^*(f; \underline{w}, \hat{\xi}_l, \boldsymbol{q}_k, \hat{\zeta}_k)}{\partial w_n} \right\}$$

$$= 2 \sum_{k=1}^{K} N_k(f) \operatorname{Re} \left\{ \varphi(f; \underline{w}, \hat{\xi}_l, \boldsymbol{q}_k, \hat{\zeta}_k) H^*(f; \boldsymbol{p}_n, \boldsymbol{q}_k, \hat{\zeta}_k) \exp \left[-i \frac{2\pi f}{c} \left(\boldsymbol{p}_n \cdot \hat{\xi}_l \right) \right] \right\}. \quad \text{(A-13)}$$

From equations (A-8) and (A-13), the nth component of the gradient of the objective function $F(\underline{w})$ is

$$\frac{\partial F(\underline{w})}{\partial w_n} = 4 \int_{f_{\min}}^{f_{\max}} V(f; \underline{w}, \hat{\xi}_l) \sum_{k=1}^{K} N_k(f) \operatorname{Re} \left\{ \varphi(f; \underline{w}, \hat{\xi}_l, \boldsymbol{q}_k, \hat{\zeta}_k) \right.$$

$$\left. H^*(f; \boldsymbol{p}_n, \boldsymbol{q}_k, \hat{\zeta}_k) \exp \left[-i \frac{2\pi f}{c} \left(\boldsymbol{p}_n \cdot \hat{\xi}_l \right) \right] \right\} df. \quad \text{(A-14)}$$

Expressions (A-6) and (A-14) for the objective function and the nth component of its gradient, respectively, are used in the optimization algorithm. These expressions are computed via numerical integration through utilization of the overlapping parabolas rule.

A-4

APPENDIX B
OVERLAPPING PARABOLAS INTEGRATION RULE

B.1 THEORETICAL DEVELOPMENT

Consider the integral $\int_a^b y(x)\,dx$, where $y(x)$ has been tabulated at unequally spaced abscissas. Let the abscissas be $a = x_1 < x_2 < x_3 < ... < x_N = b$ and let

$$P_n(x) = a_n\, x^2 + b_n\, x + c_n \ , \quad n = 2, 3, ..., N-1 \tag{B-1}$$

be the quadratic polynomial that interpolates to $y(x)$ at x_{n-1}, x_n, and x_{n+1}. An illustration of the quadratic interpolation polynomials is given in figure B-1. The integration interval (a,b) is subdivided into N subintervals (x_n, x_{n+1}), where $y(x)$ is represented as

$$y(x) \cong \begin{cases} P_2(x) \ , \quad x_1 \le x \le x_2 \\[2mm] \dfrac{1}{2}\left[P_n(x) + P_{n+1}(x) \right], \quad x_n \le x \le x_{n+1}, \ n = 2, 3, ... , N-2 \\[2mm] P_{N-1}(x) \ , \quad x_{N-1} \le x \le x_N \end{cases} \tag{B-2}$$

Note that no smoothing is done over the first and last intervals.
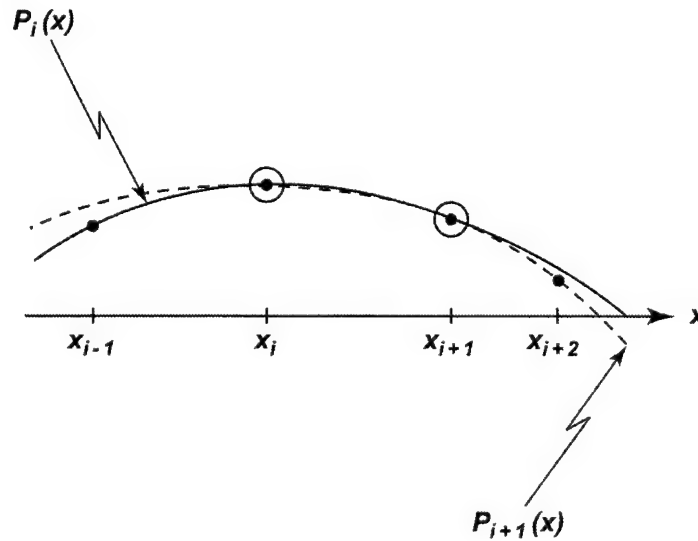
Figure B-1. Overlapping Parabolas Integration Rule

The quadratic polynomial $P_n(x)$ can be expressed as follows:

$$P_n(x) = \alpha_n (x - x_{n-1})^2 + \beta_n (x - x_{n-1}) + y_{n-1} \; , \tag{B-3}$$

where

$$\alpha_n = \frac{(x_n - x_{n-1})(y_{n+1} - y_{n-1}) - (x_{n+1} - x_{n-1})(y_n - y_{n-1})}{(x_n - x_{n-1})(x_{n+1} - x_{n-1})(x_{n+1} - x_n)} \; , \tag{B-4}$$

and

$$\beta_n = \frac{(x_{n+1} - x_{n-1})^2 (y_n - y_{n-1}) - (x_n - x_{n-1})^2 (y_{n+1} - y_{n-1})}{(x_n - x_{n-1})(x_{n+1} - x_{n-1})(x_{n+1} - x_n)} \; . \tag{B-5}$$

In the above expressions, $y_n = y(x_n)$. With the approximations in equation (B-2) for $y(x)$ over the various subintervals, the integral of $y(x)$ over (a,b) is given by

$$\int_a^b y(x)\, dx \cong \int_{x_1}^{x_2} P_2(x)\, dx + \frac{1}{2}\sum_{n=2}^{N-2}\int_{x_n}^{x_{n+1}} \left[P_n(x) + P_{n+1}(x) \right] dx + \int_{x_{N-1}}^{x_N} P_{N-1}(x)\, dx \; . \tag{B-6}$$

The above integrals can be evaluated in closed form as

$$\int_{x_1}^{x_2} P_2(x)\, dx = \int_{x_1}^{x_2} \left[\alpha_2 (x - x_1)^2 + \beta_2 (x - x_1) + y_1 \right] dx$$

$$= \alpha_2 \frac{(x_2 - x_1)^3}{3} + \beta_2 \frac{(x_2 - x_1)^2}{2} + y_1 (x_2 - x_1) \; , \tag{B-7}$$

$$\int_{x_n}^{x_{n+1}} P_n(x)\, dx = \int_{x_n}^{x_{n+1}} \left[\alpha_n (x - x_{n-1})^2 + \beta_n (x - x_{n-1}) + y_{n-1} \right] dx$$

$$= \alpha_n \left[\frac{(x_{n+1} - x_{n-1})^3}{3} - \frac{(x_n - x_{n-1})^3}{3} \right] + \beta_n \left[\frac{(x_{n+1} - x_{n-1})^2}{2} - \frac{(x_n - x_{n-1})^2}{2} \right]$$

$$+ y_{n-1} (x_{n+1} - x_n) \; , \tag{B-8}$$

B-2

$$\int_{x_n}^{x_{n+1}} P_{n+1}(x)\, dx = \int_{x_n}^{x_{n+1}} \left[\alpha_{n+1}(x-x_n)^2 + \beta_{n+1}(x-x_n) + y_n \right] dx$$

$$= \alpha_{n+1}\frac{(x_{n+1}-x_n)^3}{3} + \beta_{n+1}\frac{(x_{n+1}-x_n)^2}{2} + y_n(x_{n+1}-x_n), \qquad \text{(B-9)}$$

$$\int_{x_{N-1}}^{x_N} P_{N-1}(x)\, dx = \int_{x_{N-1}}^{x_N} \left[\alpha_{N-1}(x-x_{N-2})^2 + \beta_{N-1}(x-x_{N-2}) + y_{N-2} \right] dx$$

$$= \alpha_{N-1}\left[\frac{(x_N-x_{N-2})^3}{3} - \frac{(x_{N-1}-x_{N-2})^3}{3} \right]$$

$$+ \beta_{N-1}\left[\frac{(x_N-x_{N-2})^2}{2} - \frac{(x_{N-1}-x_{N-2})^2}{2} \right] + y_{N-2}(x_N-x_{N-1}). \text{ (B-10)}$$

The substitution of equation (B-7) through (B-10) into (B-6) gives

$$\int_a^b y(x)\, dx \cong \alpha_2\frac{(x_2-x_1)^3}{3} + \beta_2\frac{(x_2-x_1)^2}{2} + y_1(x_2-x_1)$$

$$+ \frac{1}{2}\sum_{n=2}^{N-2}\left\{ \alpha_n\left[\frac{(x_{n+1}-x_{n-1})^3}{3} - \frac{(x_n-x_{n-1})^3}{3} \right] + \alpha_{n+1}\frac{(x_{n+1}-x_n)^3}{3} \right.$$

$$+ \beta_n\left[\frac{(x_{n+1}-x_{n-1})^2}{2} - \frac{(x_n-x_{n-1})^2}{2} \right] + \beta_{n+1}\frac{(x_{n+1}-x_n)^2}{2}$$

$$\left. + (y_{n-1}+y_n)(x_{n+1}-x_n) \right\}$$

$$+ \alpha_{N-1}\left[\frac{(x_N-x_{N-2})^3}{3} - \frac{(x_{N-1}-x_{N-2})^3}{3} \right]$$

$$+ \beta_{N-1}\left[\frac{(x_N-x_{N-2})^2}{2} - \frac{(x_{N-1}-x_{N-2})^2}{2} \right] + y_{N-2}(x_N-x_{N-1}). \qquad \text{(B-11)}$$

The above expression can be simplified to

$$\int_a^b y(x)\, dx \cong \frac{1}{2}\left[\alpha_2 \frac{(x_2 - x_1)^3}{3} + \beta_2 \frac{(x_2 - x_1)^2}{2}\right]$$

$$+ \frac{1}{2}\sum_{n=2}^{N-2}\left[\alpha_n \frac{(x_{n+1} - x_{n-1})^3}{3} + \beta_n \frac{(x_{n+1} - x_{n-1})^2}{2}\right]$$

$$+ \alpha_{N-1}\left[\frac{(x_N - x_{N-2})^3}{3} - \frac{1}{2}\frac{(x_{N-1} - x_{N-2})^3}{3}\right]$$

$$+ \beta_{N-1}\left[\frac{(x_N - x_{N-2})^2}{2} - \frac{1}{2}\frac{(x_{N-1} - x_{N-2})^2}{2}\right]$$

$$+ \frac{1}{2}\left\{y_1\left[(x_3 - x_1) + (x_2 - x_1)\right] + \sum_{n=2}^{N-3} y_n (x_{n+2} - x_n)\right.$$

$$\left. + y_{N-2}\left[(x_N - x_{N-1}) + (x_N - x_{N-2})\right]\right\}.$$ (B-12)

If the abscissas are equispaced, i.e., $x_{n+1} - x_n = \Delta$, $n = 1, 2, ..., N-1$, the above expression reduces to

$$\int_a^b y(x)\, dx \cong \frac{1}{2}\left[\alpha_2 \frac{\Delta^3}{3} + \beta_2 \frac{\Delta^2}{2}\right] + \Delta^2 \sum_{n=2}^{N-2}\left[\alpha_n \frac{4\Delta}{3} + \beta_n\right]$$

$$+ \alpha_{N-1}\frac{5\Delta^3}{2} + \beta_{N-1}\frac{7\Delta^2}{4} + \frac{\Delta}{2}\left\{3y_1 + \sum_{n=2}^{N-3} 2y_n + 3y_{N-2}\right\},$$ (B-13)

where

$$\alpha_n = \frac{y_{n+1} - 2y_n + y_{n-1}}{2\Delta^2}, \quad n = 2, 3, ..., N-1,$$

$$\beta_n = \frac{-y_{n+1} + 4y_n - 3y_{n-1}}{2\Delta}, \quad n = 2, 3, ..., N-1.$$

B.2 APPLICATION TO NUMERICAL INTEGRATION OF OBJECTIVE FUNCTION

Before the overlapping parabolas integration rule could be applied to the optimal broadband array design algorithm, it had to be validated through evaluation of various integrals for which analytical results exist. The validation examples included various types of integrands, e.g., ones that were fairly smooth, oscillatory, or with cusps at one of the endpoints. In each example, the overlapping parabolas integration rule produced results that were in agreement with the analytical results, and, in most cases, the integrals converged after a reasonable number of iterations. In the examples where unequally spaced abscissas were used, the overlapping parabolas integration rule also produced satisfactory results.

As mentioned, the overlapping parabolas integration rule is to be applied in the evaluation of the objective function and its gradient at each iteration in the optimization algorithm. Before the optimization algorithm can be applied, it is necessary to know the number of frequency points required to obtain sufficiently accurate results for various weight distributions. This information is necessary because the optimization algorithm requires the transfer function at the array element locations before proceeding with the optimization calculations. In the present work, numerical convergence to seven or eight decimal places is considered adequate.

Tables B-1 through B-4 list the objective function evaluated by several integration rules for various numbers of equally-spaced frequency points for the line arrays described in figures 2a and 2b. Tables B-1 and B-3 involve the low-frequency band ($250 \text{ Hz} \leq f \leq 1000 \text{ Hz}$), and tables B-2 and B-4 involve the high-frequency band ($1723 \text{ Hz} \leq f \leq 3446 \text{ Hz}$). In each table, the objective function was computed for a uniform weight distribution because it was determined to provide convergence results that are representative of other weight distributions. Results are compared for the trapezoidal, Simpson's, and overlapping parabolas integration rules. The trapezoidal rule requires linear interpolation between abscissas, in contrast to Simpson's and the overlapping parabolas integration rules, which require quadratic interpolation. Because a quadratic interpolation between abscissas involves a smaller truncation error than for linear interpolation, Simpson's and the overlapping parabolas integration rules generally converge faster than the trapezoidal rule.

Tables B-1 and B-2 list the objective function evaluated for various numbers of frequency points across the low- and high-frequency bands, respectively, for the line array in figure 2a with a beam-steering angle of $\theta_l = 180°$. In table B-1, the objective function converges to eight decimal

places for 1000 frequency points with the overlapping parabolas rule and for between 2000 and 3000 frequency points with Simpson's rule. In contrast, with the trapezoidal rule, the objective function converges to only six decimal places for 3000 frequency points and appears to converge to seven places for 6000 frequency points. Table B-2 indicates that the objective function converges to eight decimal places for 1000 frequency points with the overlapping parabolas rule and for 2000 frequency points with Simpson's rule. In contrast, table B-2 indicates that with the trapezoidal rule the objective function converges to six decimal places with 2000 frequency points and again appears to converge to seven places for 6000 frequency points. Therefore, tables B-1 and B-2 indicate that the overlapping parabolas integration rule requires no more than 1000 frequency points to compute the objective function with eight decimal place accuracy.

Tables B-3 and B-4 list the objective function evaluated for various numbers of frequency points across the low- and high-frequency bands, respectively for the line array described in figure 2b with a beam-steering angle $\theta_l = 140°$. In table B-3, the objective function converges to seven decimal places for between 1000 and 2000 frequency points and converges to eight decimal places for between 3000 and 4000 frequency points with the overlapping parabolas rule. Table B-3 also shows that the objective function converges to eight decimal places for between 2000 and 3000 frequency points with Simpson's rule. In contrast, with the trapezoidal rule, the objective function doesn't show convergence to even six decimal places with 6000 frequency points. Table B-4 indicates that the objective function converges to eight decimal places for between 500 and 1000 frequency points with the overlapping parabolas rule and for 500 frequency points with Simpson's rule. The data in table B-4 show that with the trapezoidal rule the objective function converges to eight decimal places for between 3000 and 4000 frequency points. In summary, tables B-3 and B-4 show that the overlapping parabolas integration rule requires between 1000 and 2000 frequency points to compute the objective function with seven decimal place accuracy.

As a result of the convergence tests of the objective functions, it was determined that approximately 1000 to 2000 frequency points are sufficient for seven to eight decimal place accuracy with the overlapping parabolas integration rule. Similar convergence tests for the gradient terms (not shown here) have also been performed with similar convergence results as the objective function. It should also be mentioned that all computations performed in this report involve double-precision accuracy (i.e., 15 decimal places). In each of the examples described in this report, the optimization results were obtained with at least 2000 frequency points.

***Table B-1. Convergence Test of the Objective Function with Several Numerical Integration
Procedures for the Line Array in Figure 2a in the Low-Frequency
Band (250 Hz ≤f ≤1000 Hz) with Uniform Weights and a
Beam Steered at the Look Angle $\theta_l = 180°$***

No. of Frequency Points	Overlapping Parabolas Rule	Trapezoidal Rule	Simpson's Rule
100	2.6294267×10^{10}	2.6296756×10^{10}	2.6265587×10^{10}
250	2.6293594×10^{10}	2.6294086×10^{10}	2.6293237×10^{10}
500	2.6293547×10^{10}	2.6293679×10^{10}	2.6293508×10^{10}
1000	2.6293543×10^{10}	2.6293577×10^{10}	2.6293539×10^{10}
2000	2.6293543×10^{10}	2.6293551×10^{10}	2.6293542×10^{10}
3000	2.6293543×10^{10}	2.6293547×10^{10}	2.6293543×10^{10}
4000	2.6293543×10^{10}	2.6293545×10^{10}	2.6293543×10^{10}
6000	2.6293543×10^{10}	2.6293543×10^{10}	2.6293543×10^{10}

***Table B-2. Convergence Test of the Objective Function with Several Numerical Integration
Procedures for the Line Array in Figure 2a in the High-Frequency
Band (1723 Hz ≤f ≤3446 Hz) with Uniform Weights and a
Beam Steered at the Look Angle $\theta_l = 180°$***

No. of Frequency Points	Overlapping Parabolas Rule	Trapezoidal Rule	Simpson's Rule
100	7.4848970×10^{9}	7.4832128×10^{9}	7.4848169×10^{9}
250	7.4843096×10^{9}	7.4841299×10^{9}	7.4843449×10^{9}
500	7.4843014×10^{9}	7.4842584×10^{9}	7.4843065×10^{9}
1000	7.4843010×10^{9}	7.4842904×10^{9}	7.4843017×10^{9}
2000	7.4843010×10^{9}	7.4842983×10^{9}	7.4843010×10^{9}
3000	7.4843010×10^{9}	7.4842998×10^{9}	7.4843010×10^{9}
4000	7.4843010×10^{9}	7.4843003×10^{9}	7.4843010×10^{9}
6000	7.4843010×10^{9}	7.4843007×10^{9}	7.4843010×10^{9}

Table B-3. *Convergence Test of the Objective Function with Several Numerical Integration Procedures for the Line Array in Figure 2b in the Low-Frequency Band (250 Hz $\leq f \leq 1000$ Hz) with Uniform Weights and a Beam Steered at the Look Angle $\theta_l = 140°$*

No. of Frequency Points	Overlapping Parabolas Rule	Trapezoidal Rule	Simpson's Rule
100	9.6152579×10^7	9.6340542×10^7	9.6011845×10^7
250	9.6455449×10^7	9.6442003×10^7	9.6469275×10^7
500	9.6465930×10^7	9.6460253×10^7	9.6466297×10^7
1000	9.6466205×10^7	9.6464721×10^7	9.6466206×10^7
2000	9.6466201×10^7	9.6465831×10^7	9.6466201×10^7
3000	9.6466201×10^7	9.6466036×10^7	9.6466200×10^7
4000	9.6466200×10^7	9.6466108×10^7	9.6466200×10^7
6000	9.6466200×10^7	9.6466159×10^7	9.6466200×10^7

Table B-4. *Convergence Test of the Objective Function with Several Numerical Integration Procedures for the Line Array in Figure 2b in the High-Frequency Band (1723 Hz $\leq f \leq 3446$ Hz) with Uniform Weights and a Beam Steered at the Look Angle $\theta_l = 140°$*

No. of Frequency Points	Overlapping Parabolas Rule	Trapezoidal Rule	Simpson's Rule
100	8.9649025×10^8	8.9648170×10^8	8.9649436×10^8
250	8.9649006×10^8	8.9648870×10^8	8.9649011×10^8
500	8.9649001×10^8	8.9648868×10^8	8.9649000×10^8
1000	8.9649000×10^8	8.9648990×10^8	8.9649000×10^8
2000	8.9649000×10^8	8.9648998×10^8	8.9649000×10^8
3000	8.9649000×10^8	8.9648999×10^8	8.9649000×10^8
4000	8.9649000×10^8	8.9649000×10^8	8.9649000×10^8
6000	8.9649000×10^8	8.9649000×10^8	8.9649000×10^8

REFERENCES

1. R. L. Streit, "Optimization of Discrete Arrays of Arbitrary Geometry," *Journal of the Acoustical Society of America*, vol. 69, no. 1, January 1981, pp. 199-212.

2. R. L. Streit and A. H. Nuttall, "A General Chebyshev Complex Function Approximation Procedure and an Application to Beamforming," *Journal of the Acoustical Society of America*, vol. 72, no. 1, July 1982, pp. 181-190.

3. B. A. Cray, "Amplitude Shading Coefficients for Highly-Curved Apertures," CAVES Signal Processing Working Group Presentation, Naval Undersea Warfare Center Division, New London, CT, 21 May 1996.

4. R. L. Streit and T. A. Wettergren, "An Objective Function for Optimal Hull Array Design Using a Broadband Detection Criterion," NUWC-NPT Technical Memorandum 990124, Naval Undersea Warfare Center Division, Newport, RI, 15 December 1999.

5. M. C. Junger and D. Feit, *Sound, Structures, and Their Interaction*, Second Edition, MIT Press, Cambridge, MA, 1986, pp. 228-233, 249-250, 279-289.

6. P. Stepanishen and T. A. Wettergren, "Structural-Acoustical Analysis of a Point Excited Fluid-Loaded Spherical Shell," NUWC-NPT Technical Memorandum 00-003, Naval Undersea Warfare Center Division, Newport, RI (in preparation).

7. P. E. Gill, W. Murray, M. A. Saunders, and M. H. Wright, "User's Guide for NPSOL (Version 4.0): A Fortran Package for Nonlinear Programming," Technical Report SOL 86-2, Department of Operations Research, Stanford University, Stanford, CA, January 1986.

8. R. Fletcher, *Practical Methods of Optimization*, Second Edition, J. Wiley and Sons, New York, 1987, pp. 304-317.

9. J. Nocedal and S. J. Wright, *Numerical Optimization*, Springer-Verlag, New York, 1999, Ch. 18.

10. J. P. Casey and R. L. Streit, "Beam Synthesis of Conformal Antenna Arrays," NUWC-NPT Technical Report, Naval Undersea Warfare Center Division, Newport, RI (in preparation).

11. P. J. Davis and P. Rabinowitz, *Numerical Integration*, Blaisdell Publishing Co., Waltham, MA, 1967, pp. 22-24.

12. Private communication with Professor Peter Stepanishen, Dept. of Ocean Engineering, University of Rhode Island, Narragansett, RI, May 1999.

13. A. Papoulis, *Probability, Random Variables, and Stochastic Processes*, McGraw-Hill, New York, 1965, p. 338.

INITIAL DISTRIBUTION LIST

Addressee	No. of Copies
Space and Naval Warfare Systems Center (P. Hansen, R. Dinger)	2
Office of Naval Research (ONR-313: W. Stachnik, J. Freebersyer)	2
Defense Technical Information Center	2
Center for Naval Analyses	1
Science Applications International Corporation (R. Ingram, D. Miller, E. Wolkoff)	3
University of Connecticut (R. Bansal)	1
University of Rhode Island (P. Stepanishen)	1
University of Maryland (H. Elman)	1